INFORMATION TO USERS

This manuscript has been reproduced from the microfilm master. UMI films the text directly from the original or copy submitted. Thus, some thesis and dissertation copies are in typewriter face, while others may be from any type of computer printer.

The quality of this reproduction is dependent upon the quality of the copy submitted. Broken or indistinct print, colored or poor quality illustrations and photographs, print bleedthrough, substandard margins, and improper alignment can adversely affect reproduction.

In the unlikely event that the author did not send UMI a complete manuscript and there are missing pages, these will be noted. Also, if unauthorized copyright material had to be removed, a note will indicate the deletion.

Oversize materials (e.g., maps, drawings, charts) are reproduced by sectioning the original, beginning at the upper left-hand corner and continuing from left to right in equal sections with small overlaps.

Photographs included in the original manuscript have been reproduced xerographically in this copy. Higher quality 6" x 9" black and white photographic prints are available for any photographs or illustrations appearing in this copy for an additional charge. Contact UMI directly to order.

Bell & Howell Information and Learning
300 North Zeeb Road, Ann Arbor, MI 48106-1346 USA
800-521-0600

UMI®

Observation of bilayer growth in the initial epitaxy of pseudomorphic Mg on Mo(001)

by

David Droppo ©

Abstract

The epitaxy of Mg, a hexagonal-close packed metal in the bulk, onto a body-centered-cubic Mo(001) substrate throughout a range of temperatures from room temperature to 450 K is investigated. The Mg grows in a Stranski-Krastanov mode where the first four layers grow as pseudomorphic fcc Mg followed by a transition to 3D growth. LEED and AES are used to investigate the Mg film during the pseudomorphic growth. Initially the film is observed to grow as a bilayer. This is attributed to the presence on an energy barrier preventing interlayer mass transport. For the first two monolayers of coverage the film grows via island nucleation due to the highly corrugated surface potential of the bcc surface. The third and fourth layer grow via step flow. The increased diffusion constant necessary for step flow is due to the compressive strain of the bilayer.

Table of Contents

CHAPTER 1

Introduction

Epitaxial growth of thin films on solid substrates is of great interest because it allows for the creation of materials with morphologies and chemical compositions which are not found in nature. The size of electronic devices is continually being decreased to minimize space requirements. Surface related phenomena become more important in the design of these devices as the surface to volume ratio continues to increase. Metal surfaces are very important to the development of heterogeneous catalysis. Often very expensive metals are used. Since catalysis is purely a surface phenomenon the cost can be greatly reduced by growing thin clusters of this expensive metal onto the surface of a more inexpensive one. Metal on metal films are also used for data storage. Large resistive changes in a magnetic field for certain devices composed of alternating thin layers of metals are being used to create the next generation of disk drives. A greater understanding of the properties of surfaces is crucial to the development of these areas.

Today many technologies rely on the routine fabrication of ultrathin epitaxial layers. One of the fundamental issues governing epitaxial growth is how the lattice mismatch between film and substrate material induces structural modifications in the growing film. A film grows pseudomorphically when it adopts the crystal structure and lattice constant of the substrate. The strain which results from pseudomorphic growth may have a strong impact on the film morphology.

In this study the growth of Mg on the Mo(001) surface is investigated between room temperature and 450 K. Molybdenum is chosen as the substrate because the body-centered cubic surface is highly corrugated. The corrugated surface potential can induce pseudomorphic growth in the initial layers of deposition. Magnesium was chosen as the

deposit since it has a nearest neighbour separation of 3.21 Å which compares favourably with the lattice parameter of Mo, 3.15 Å. Also the surface energy (the energy required to create the surface) of Mg is much lower than that of Mo, which thermodynamically favours layer-by-layer film growth.

In fact previous results at room temperature show that four layers of Mg grow pseudomorphically, followed by a transition to hexagonal Mg(0001) (Wu, 1992). Within the first four layers the third and fourth layer grow by step flow whereas the first two grow via island nucleation (Gallagher, 1999). This last study used STM measurements which were all made in excess of 1 hour after deposition. This was particularly troublesome at low coverage (less than two monolayers) where the film became oxidized.

This work builds on previous results and concentrates on the growth in the pseudomorphic regime (up to four monolayers). Experimental techniques used here include Low Energy Electron Diffraction (LEED) and Auger Electron Spectroscopy (AES). These two techniques have the advantage that they can be performed immediately after deposition. This significantly reduces the oxidation of the Mg film making it possible to effectively investigate low coverages. This study also expands on previous work (Wu, 1992)(Gallagher, 1999), which was all done at room temperature, to examine the growth throughout a range of substrate temperatures from room temperature to 450 K.

In this study it is found that the first Mg layer grows as a bilayer throughout the temperature range investigated and the transition to 3D growth occurrs after the completion of the fourth layer.

This thesis is organized into chapters as follows. Chapter 2 provides an overview of the theory of film growth. The information presented will be used later in chapter 4 to interpret the results of the experiments. Chapter 3 presents the details of the vacuum system in which the experiments were performed as well as information on the analytical tools used to collect the data. In chapter 4 the results are presented. This chapter also includes a discussion in which possible driving forces behind the results are discussed. Finally, the conclusion presents a summary of the results of this study.

CHAPTER 2

Theory of Film Growth

Introduction

In microelectronics it is often desired to create a heterostructure of two different materials that may differ significantly in lattice constant and crystal structure. Heteroepitaxy refers to the growth of an oriented single crystal film of one material onto a single crystal substrate of another.

Growth Modes

There are three distinct growth modes for epitaxial growth each named for the scientists who first investigated them (Bauer, 1958).

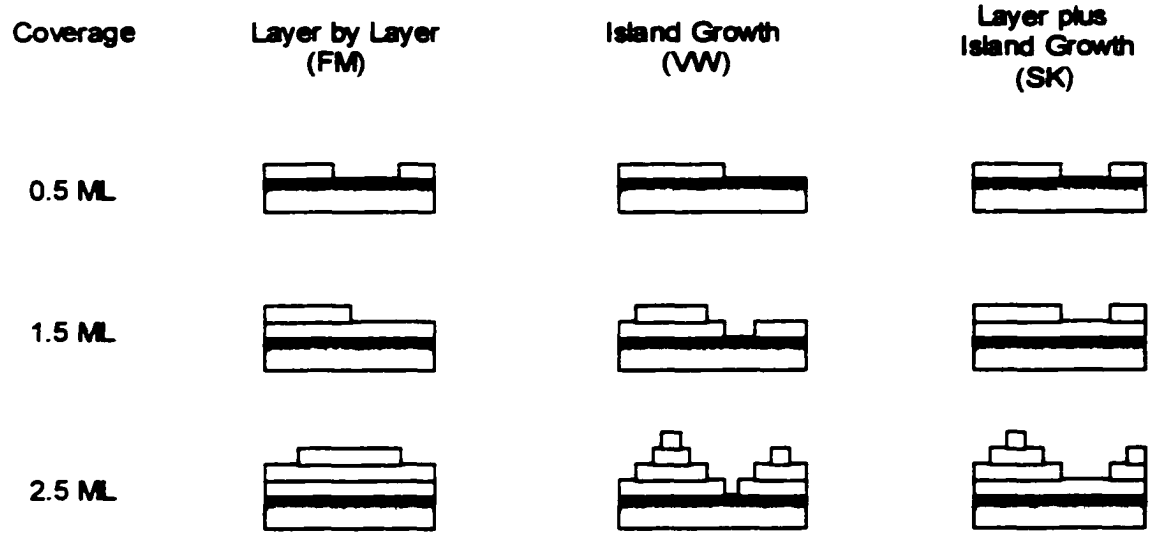

Figure 2.1 The evolution of the three distinct epitaxial processes at different coverages (in monolayers or ML)

The layer by layer growth mode is referred to as FM (Frank-van der Merwe). In this mode a new layer does not start to form until the previous one is complete. This mode is frequently observed in the growth of semiconductors on semiconductors and some metal-metal systems (Venables, 1984).

The island growth mode is referred to as VW (Vollmer-Weber) and is the opposite case. In this mode the equivalent of many monolayers must be deposited before the substrate is entirely covered because the islands grow to be quite tall before they coalesce to cover the surface. This growth mode is common when growing metals on insulators (Venables, 1984).

The layer plus island growth mode (or SK for Stranski-Krastanov) is an interesting intermediate case. The deposited atoms initially form in a layer mode but after one or more layers this growth mode becomes unfavourable and any subsequent deposit atoms will nucleate to form islands. This growth mode is the most common and there are many examples of this for metal-metal and metal-semiconductor systems (Venables, 1984).

Thermodynamic Predictions

One explanation for the different growth modes relies on considering the thermodynamic properties of the system. The surface energy γ is defined as the surface excess free energy per unit area to create the surface. The total energy of the system is the sum of three parts, the surface energy of the film γ_f, the surface energy of the substrate γ_s, and the surface energy of the substrate-film interface γ_i. If $\gamma_f + \gamma_i$ is greater than γ_s, the film will grow in 3D islands to expose more of the surface thus minimizing

the total energy. Conversely if $\gamma_f + \gamma_i$ is less than γ_s a similar argument leads to the reasoning that the film will grow in layers. For layer by layer growth this condition must be satisfied for every subsequent layer of the deposit so this growth mode occurs only when the film and substrate are very similar so that $\gamma_f \approx \gamma_s$ and $\gamma_i \approx 0$. In homoepitaxy those approximations turn to equalities (Merwe, 1994).

It is still difficult to predict in which mode two differing materials will grow for two reasons. First of all, it is unclear what the value for γ_i is for any epitaxial pair and second γ_f is not necessarily the same as the surface energy of the bulk material.

Kinetic Factors

The greatest limitation of the thermodynamic treatment is that film growth is not an equilibrium process. The flux of incident atoms and the mobilities of these adatoms are among the necessary kinetic considerations. A surface consists of atomically flat terraces separated by steps that are typically one atom in height. Once an atom has condensed onto the surface it will diffuse around different adsorption sites. It will stop migrating in one of two ways.* Due to higher coordination it can attach itself to a step edge. Alternatively, it can nucleate and form an island upon meeting other condensed atoms as shown in Figure 2.2. In general adsorbate islands are continuously forming and dissociating until an island reaches a certain critical size of atoms were it is effectively stable. However this critical island size is only one atom for most metal on metal systems even at high temperatures (Hwang, 1997).

* Other processes can occur but are not going to be considered in this simplified case. They include the re-evaporation of adatoms or interdiffusion between adsorbate and substrate layer.

When adatoms predominantly attach themselves to step edges the film grows by step flow. During step flow the film grows in the FM growth mode where the substrate morphology is preserved with the completion of each layer.

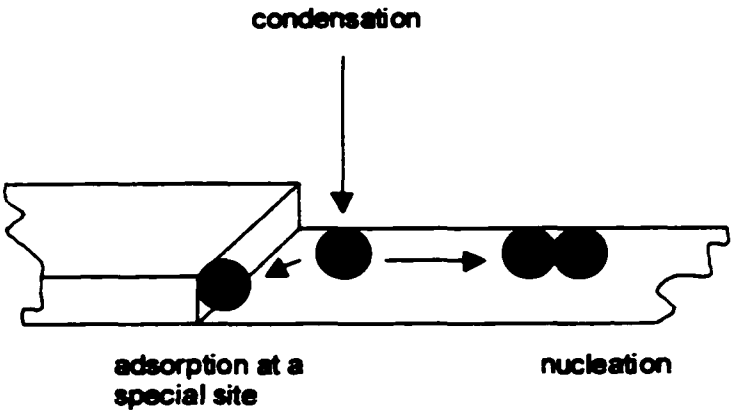

Figure 2.2 The two ways in which a condensed atom can be adsorbed onto the substrate surface

Under certain conditions, such as high flux or low diffusion rate, adatoms are more likely to meet and nucleate as islands rather than to migrate to the step edge. This growth process is called island nucleation. Figure 2.3 shows the two growth processes of step flow and island nucleation.

Temperature also plays an important role in determining which growth process will dominate since the diffusion rate of condensed atoms along the surface is intimately related to the substrate temperate. If the substrate were cooled the diffusion rate would be lower and island nucleation would be favoured.

The growth can also depend on the deposition flux. For example a high flux would favour island nucleation since adatoms are more likely to encounter each other before they can attach to a step edge regardless of the adatom mobility.

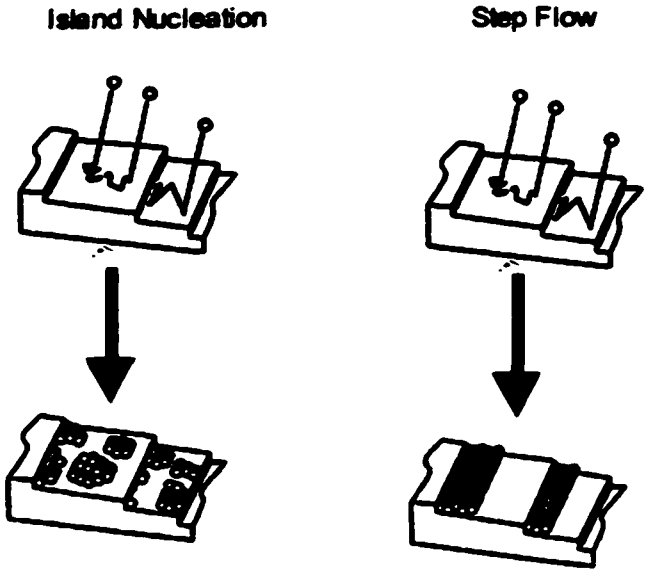

Figure 2.3 The two growth processes of island nucleation and step flow

Other Factors

Impurities have also been shown to greatly effect film growth both thermodynamically and kinetically. Thermodynamically, an impurity on the surface of a substrate will alter the value of γ_s. This may change the lowest energy configuration from layer-by-layer to 3D island growth or vice versa. Kinetically, adatoms must displace impurity atoms in order to migrate and this can lead to slower diffusion rates. This effect was studied in the growth of Au on Ru(0001) where the substrate was deliberately pre-covered with oxygen (Schroder, 1992). It was found that the density of Au islands increased by four orders of magnitude in the presence of oxygen. In other systems impurities such as oxygen can have the reverse effect. Precovering the substrate with a small amount of oxygen can enhance layer-by-layer growth. This was shown in the homoepitaxy of Pt onto Pt(111) (Esch, 1994). It was concluded that oxygen reduces

the effective barrier at a step edge thus making it easier for the Pt atoms to descend to a lower layer. This increase interlayer transport will encourage layer growth.

The mobility of the adsorbed atoms can be a function of film thickness for some systems. For Ni grown on Ru(0001) (Meyer, 1995) it was found that the mobility of Ni adatoms increases with film thickness. At low coverages the film is highly corrugated and 3D growth occurs via island nucleation. At higher coverages strain relaxation increases mobility encouraging interlayer transport to produce a much smoother film. An increased mobility is also observed in the Mg on Mo(001) system as seen in the transition from island nucleation to step flow growth (Gallagher, 1999).

Lattice Strain in Film Growth

A key factor in determining the structure of a growing film is lattice mismatch. A lattice mismatch between the adsorbate and substrate crystal presents an interesting problem for the growing film. The adatoms prefer to sit in the minima of the substrate corrugation potential however the film strives to maintain the crystal structure and lattice spacing of its bulk structure.

The competition results in many different film structures. In the pseudomorphic mode the film adopts the structure and lattice spacing of the substrate. This mode can be encouraged by depostion onto a highly corrugated substrate surface. To counter the lateral strain the vertical lattice spacing will often change in the opposite direction due to elastic relaxation as shown in Figure 2.4 a). As the film thickens the strain energy increases. One way to relieve strain is the formation of dislocations at the interface as shown in Figure 2.4 b).

For a weakly corrugated substrate the film may grow with no strain. This results in floating mode shown in Figure 2.4 c). In this case the film maintains the lattice constant of the bulk material.

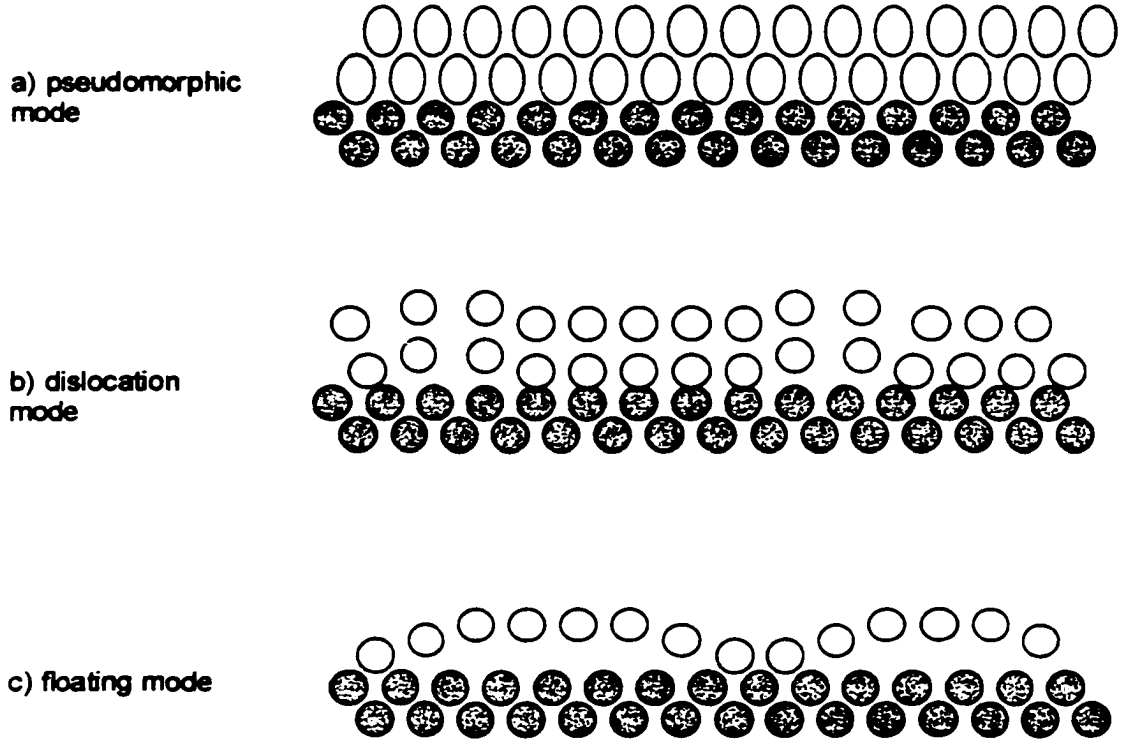

Figure 2.4 Three different modes of growth for the first few monolayers of heteroepitaxial growth (Henzler, 1995)

Pseudomorphic Growth

A film is said to grow pseudomorphically if it adopts the crystal structure and lattice spacing of the substrate (Zangwill, 1988). The film does so at the expense of strain energy if the substrate structure or lattice spacing of the substrate is different than the deposit. As the film grows the strain energy increases until at some critical thickness it is energetically favourable to relieve the strain. Strain relief in the film can be

accomplished by forming dislocations (Figure 2.4 b) but an alternative method is a change in growth mode from layer growth to 3D island growth. i.e. SK growth mode (Merwe, 1994).

In pseudomorphic growth one must consider the strain energy as well as the surface energy of the system to predict the growth mode. The total energy per unit area will then be the sum of the surface free energies per unit area, γ, and the strain energy per unit area, ε. The total energy per unit area can then be written (van der Merwe, 1994) as:

$$E_j = \gamma_j + \varepsilon_j \tag{2.1}$$

Where j= s, ML, DL and s is the substrate, ML is the first monolayer and DL is the doublelayer. $E_s = \gamma_s$ for the substrate since it is not strained. Consider a system with the substrate, first layer and second layer exposed shown in Figure 2.5. The change in energy which results from the transfer of material from the second layer to the first layer or $\Delta E_{DM,ML}$ can be written as

$$\Delta E_{DM,ML} = 2E_{ML} - E_{DL} - E_s \tag{2.2}$$

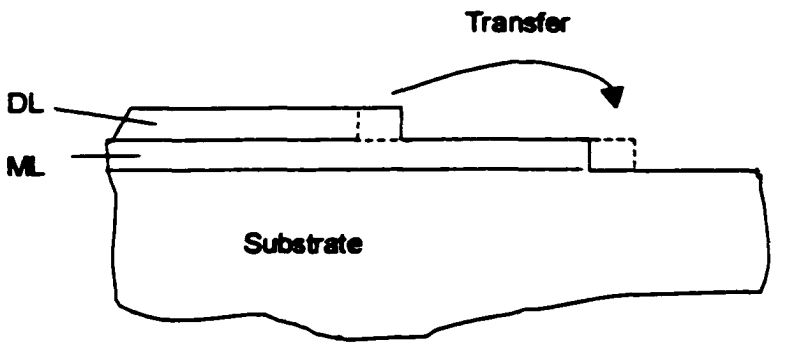

Figure 2.4 The transfer described in equation (2.2).

This can be seen from Figure 2.4 where the $2E_{ML}$ is added due to the additional expsosed surface of the first monolayer. The $-E_{DL}$ is from the removal of part of the second layer and the $-E_S$ results from covering of part of the substrate.

Similar definitions can be used for a general expression

$$\Delta E_{n+1,n} = 2E_n - E_{n+1} - E_{n-1} \tag{2.3}$$

Layer-by-layer growth is observed as long as $\Delta E_{ML,DL} \leq 0$. Island growth is expected when $\Delta E_{n+1,n} > 0$. The critical layer thickness n_c and the S-K transition to 3D growth occurs when $\Delta E_{n+1,n}$ becomes positive.

Mg on Mo(001)

The surface energies of Mo(001) and Mg(0001) have been calculated to be 3.8737 and 0.7292 Jm^{-2} respectively (Vitos, 1998). Since the surface free energy of the substrate is larger than the film, thermodynamically one would expect the Mg to grow in a layer-by-layer fashion. The small lattice mismatch and the highly corrugated potential energy of the bcc(001) surface (Bauer, 1982) implies that the initial Mg layers should grow pseudomorphically. As the lattice mismatch is only 2% and the difference in surface energies is so large one would expect the Mg to grow as a strained film for several layers.

CHAPTER 3

Experimental Apparatus & Procedure

3.1 Ultra High Vacuum

The Need for UHV

In order to effectively study a surface it is of great importance that the state of the surface remains constant over the duration of an experiment. The need to keep a sample clean means that the arrival rates of molecules impinging on the surface of the sample should be low. It is this requirement for ultra-low pressures that had hindered surface physics until the advent of ultra-high vacuum (UHV) technology. Since the early 1960s the commercial availability of UHV systems and components has played a major role in the recent successes in surface physics.

The operating pressure inside a UHV system is typically 1×10^{-10} torr. Calculating how long a surface can be kept clean at a given pressure can be done easily from kinetic gas theory. The time for one complete monolayer of molecules to condense on the sample is a function of the arrival rate of the molecules Γ and the surface area that the molecules occupy, d_0. It can be calculated by the following equation (O'Hanlon, 1989):

$$t_{ml} = \frac{4kT}{Pvd_0^2} \tag{3.1}$$

where the arrival rate has been expressed in terms of the temperature T, the average velocity v, the pressure P, and Boltzmann's constant k. Using d_o for air as 0.372 nm and v as 467 m/s at room temperature under UHV conditions it will take over 5 hours to cover the sample. A clean sample will not acquire much contamination for the duration of an experiment. At atmospheric pressure a clean surface would be covered after only 25 ns and in a very high vacuum, typically in the range of 10^{-7} torr to 10^{-9} torr, the sample

would only stay clean for 4 minutes. Clearly, UHV pressures are needed to successfully keep the surface clean for any practical length of time.

How UHV is Attained

For these experiments UHV is attained using the apparatus shown in Figure 3.1. The main components of the system (as with any UHV system) are the pumps. Different pumps are required because no one pump will work for the entire range of pressures between atmosphere and UHV. This is shown in Figure 3.2. Also different pumps pump

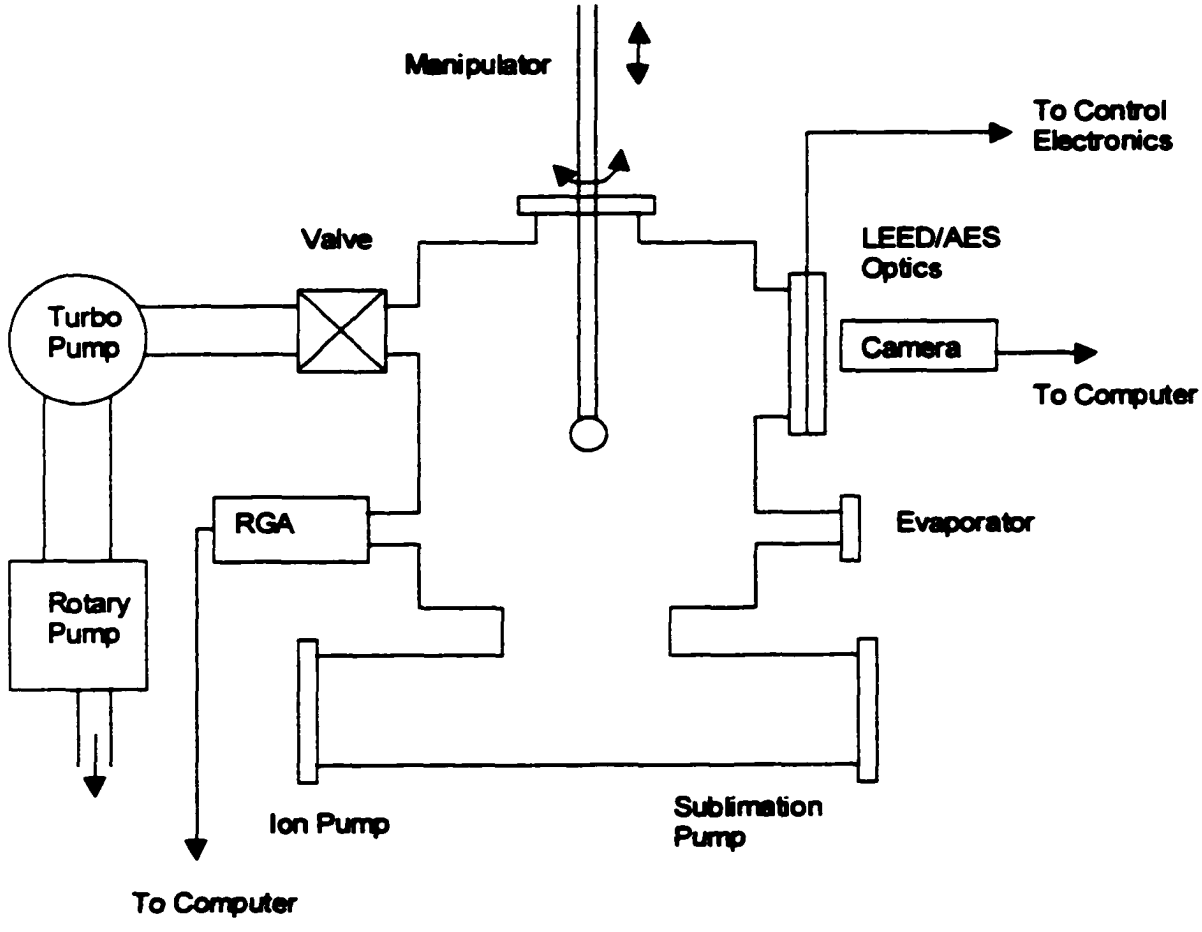

Figure 3.1 A schematic of the UHV system used.

different gases with varying degrees of efficiency. The rotary pump removes air from the chamber by expelling it into the atmosphere. It has a high pumping speed but it has a low pressure limit of only 10^{-3} torr. The next stage of pumping is a turbomolecular pump (another displacement pump but with a lower pumping speed of 60 L/s). It pumps gas

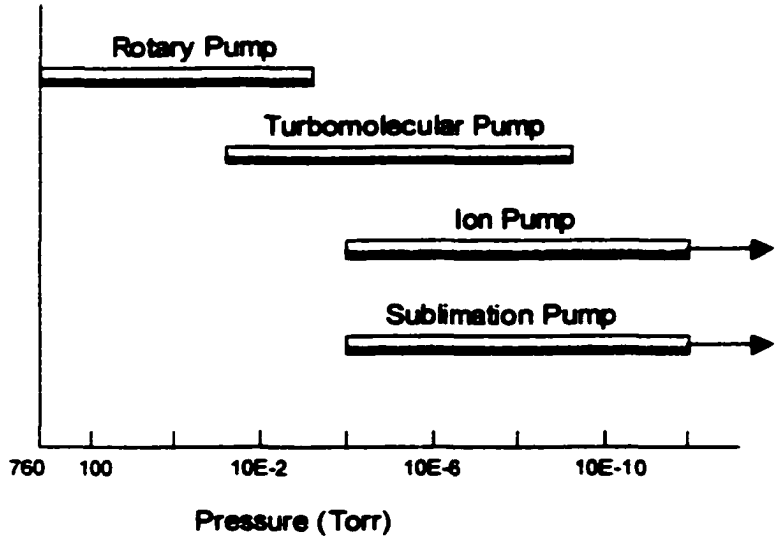

Figure 3.2 The ranges of pressure for which the different pumps are used

using momentum transfer by fast rotating blades at 70 krpm. The turbo can be used to pump to its ultimate pressure of $1x10^{-9}$ torr (Varian Vacuum Products, 1997) but it cannot exhaust the air to atmosphere. It is therefore backed by the rotary pump. To achieve a lower pressure the turbomolecular pump and rotary pump must be valved off. At low pressure the ion pump ionizes molecules and accelerates them to a high velocity so that when they strike a titanium wall they are buried. In the process of burying themselves in the wall, the ions sputter Ti leaving the Ti to getter active gases. The pumping speed of our ion pump is 110 L/s. A titanium sublimation pump (TSP) can also be used to pump

in the UHV pressure range. Titanium is evaporated and deposited on adjacent walls. The titanium film is water-cooled and active gases (water vapor, oxygen, etc) are captured. Once this film surface is contaminated with adsorbed gases a fresh titanium film can be deposited on top. The pumping speed of the TSP is calculated at over 10000 L/s. Its effective pumping speed is considerably less than this because it is limited by the conductance of the gases through the 6 inch flange that connects the TSP to the chamber. The conductance of the flange is calculated to be just over 2000 L/s (O'Hanlon, 1989).

Despite the high pumping speed of this network of pumps, 10^{-8} torr would be the ultimate base pressure without baking the system (Luth, 1993). When the chamber walls are exposed to the atmosphere water vapor adsorbs on the walls of the chamber and absorbs into the walls of the chamber. When the system is then being pumped down these water molecules slowly desorb and limit the ultimate pressure of the system. Baking the chamber to 100°C for 48 hours thermally desorbs the water vapor from the walls and diffuses the water from inside the walls thus allowing it to be pumped out of the chamber.

Residual Gas Analyzer

One of the key instruments in the vacuum system is the residual gas analyzer (RGA). The RGA is a mass spectrometer that has enough resolution to clearly distinguish between atomic mass peaks that are 1 amu apart. If the operating pressure of the system is higher than expected, then a mass spectrum using the RGA can diagnose the problem. An RGA scan can lead to valuable information about oil contamination (backstreaming from the roughing pump), solvent contamination (solvents such as

acetone used for cleaning parts in the vacuum), an air leak (characterized by a large nitrogen peak) and outgassing from components within the system (Stanford Research Systems, 1996). An example of a mass spectra is shown in Figure 3.3. During an experiment the RGA was also used to calibrate the flux of the deposit but this will be discussed later.

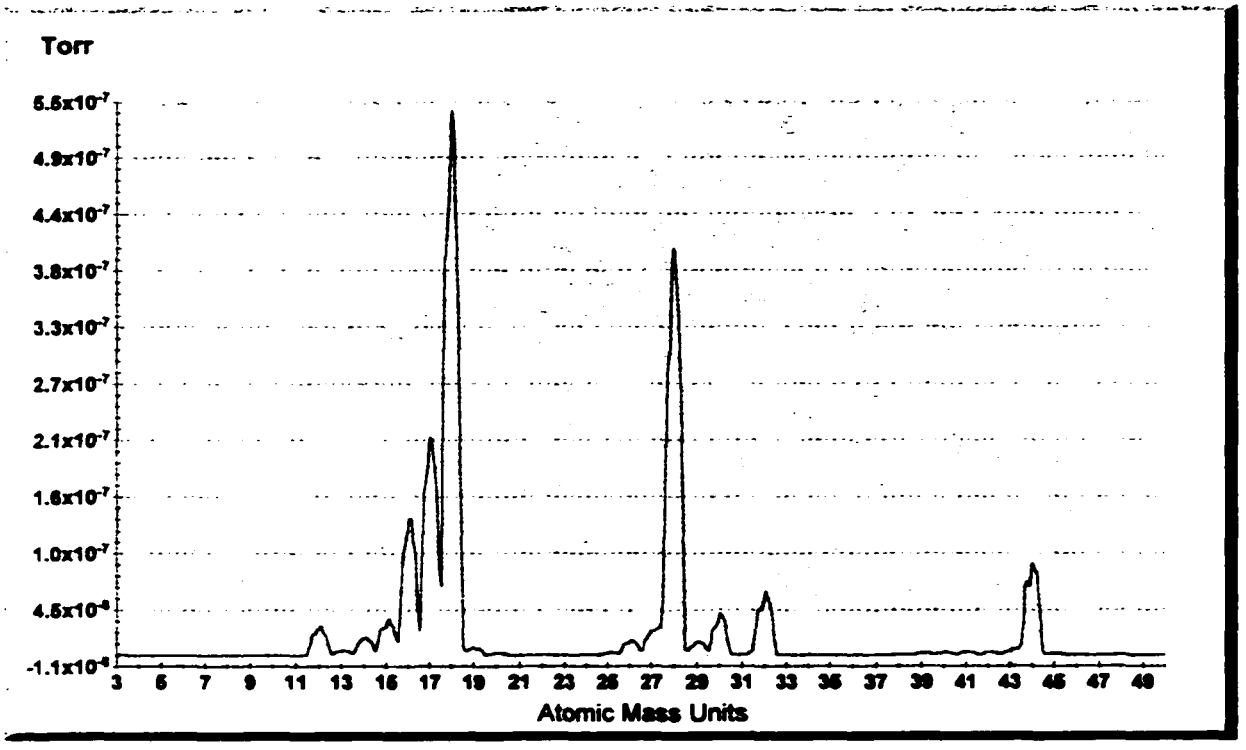

Figure 3.3 A mass sectra taken by the RGA before baking the system. The main gas in the system is water vapour (as seen by the large peak at 18 amu) from the outgassing of the chamber walls.

Sample Mounting

Once UHV has been attained the system is ready to perform experiments. The single crystal molybdenum sample was purchased from Princeton Scientific Corporation. The sample is 10mm in diameter and 1mm in thickness. The surface is Mo(001) $\pm$ 0.5° and was mechanically polished with 1μ diamond paste. The sample is placed on a

manipulator that allows for translational and rotational movement so that the sample can be aligned in front of the different apparatus within the vacuum system. The sample is mounted so that it is electrically and thermally isolated to allow for heating. The sample mounting is shown is Figure 3.4. A current is passed through a filament that is in close proximity to the sample. The sample is then biased to a high positive potential so that the electrons emitted from the filament are accelerated toward the sample and bombard the sample with a high velocity thus heating the sample. Both the filament current and the bias can be adjusted to attain different temperatures of the sample. The temperature of

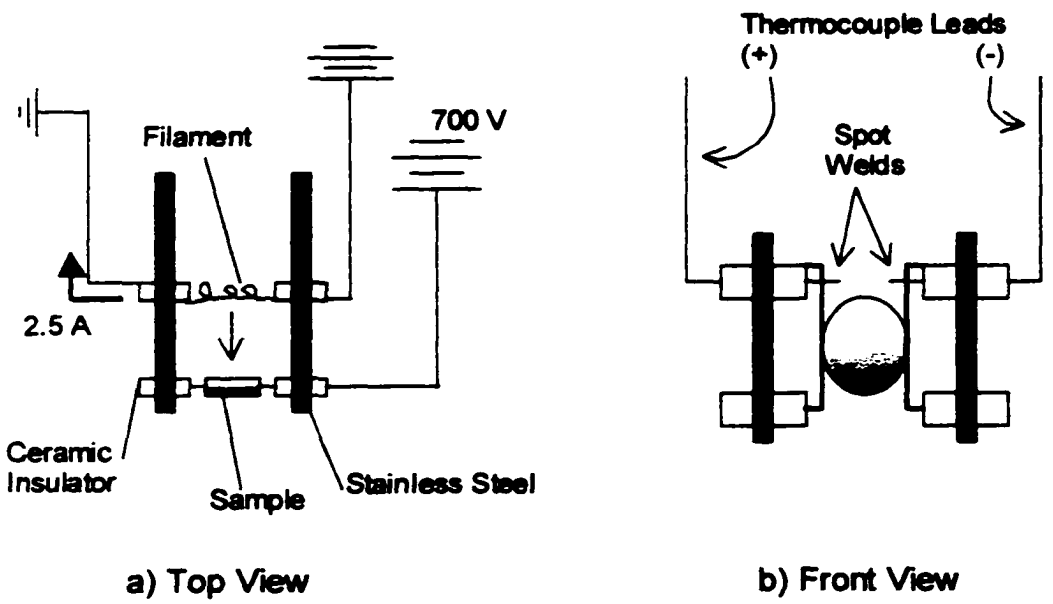

Figure 3.4 The sample mounting. (a) shows how the sample is heated. (b) shows how that thermocouple is attached to the sample.

the sample is measured in two ways. If the sample is at a temperature of 1000°C or above an optical pyrometer can be used. Temperatures below this are measured using a thermocouple mounted near the sample. Tungsten 5% rhenium(+) and tungsten rhenium

26% (-) is used as the thermocouple because of its high melting point of over 2315°C (Omega Engineering, 1995). After repeated failures in attempting to spot weld the thermocouple to the sample, it was moved to the connecting wires that are very close in temperature to the sample. The thermocouple is then calibrated to the temperature of the sample. At room temperature the thermocouple gives a reading of 0 mV. Measuring the thermocouple voltage as Mg is thermally desorbed gives a reading at 500 K (approximately 3.1 mV). Additional calibration can be attained at higher temperatures by comparing the thermocouple with pyrometer readings.

Cleaning the Sample

The next challenge is to obtain an atomically clean surface on which to do experiments. Heating alone cannot be used to thermally desorb contaminants that are strongly bound to the sample's surface such as carbon. However the introduction of oxygen into the vacuum will displace the contaminants by oxidizing the sample at an elevated temperature. The oxygen is then removed by thermal desorption.

The molybdenum sample is cleaned by heating it to 800°C in a backpressure of oxygen at $1x10^{-7}$ torr for 5 minutes. 800°C was achieved by running 2.75A through the filament (shown in Figure 3.4a) and biasing the sample to 300 V. After the oxygen had been pumped out of the chamber the sample was flashed to 1700°C to desorb the oxygen from the surface. Running 3.5A through the filament and biasing the sample to 800V attained this temperature. This process is repeated until the surface is satisfactorily clean as determined by looking at the LEED image and AES.

Evaporating Mg onto Mo(001)

After the Mo surface is satisfactorily cleaned, the next step is to grow Mg films. Mg is evaporated by wrapping Mg ribbon (0.15mm thick and 3mm wide) around a wire that is electrically isolated from the chamber. The magnesium ribbon is from Aldrich Chemical Company Inc. and has a purity 99+ %. Passing current through the wire heats the wire that in turn heats the Mg so that it sublimes. By varying the current the Mg flux is adjusted. Typically a current of 5.5A is used to create a Mg vapour pressure of 2.5×10^{-9} torr. From the vapour pressure of Mg, this implies that the ribbon is being heated to 530 K (O'Hanlon, 1989). The flux is equivalent to 0.66 ML/min as calibrated by subsequent LEED and AES data. It is varied between 0.5-1ML/min for different experiments. The flux is measured by examining the 24 amu peak on the RGA that was strategically placed (as shown in Figure 3.1) directly across from the evaporator. To grow the films the sample is lowered into the beam of Mg flux. Different film thicknesses are attained by varying the amount of time that the sample spends in the Mg flux. Films are deposited at elevated substrate temperatures by passing a current through the sample filament shown in Figure 3.4 a) and allowing the radiation to heat the sample.

3.2 Low Energy Electron Diffraction (LEED)

Introduction

LEED is the oldest of all surface science techniques. The technique takes advantage of the wave nature of the electrons by forming a Fraunhofer diffraction pattern of electrons that are elastically backscattered from the crystal surface. In 1927 a LEED experiment first demonstrated the wave nature of the electron. The experiment by Davisson and Germer ultimately won the Nobel Prize in 1937. The diffraction is possible

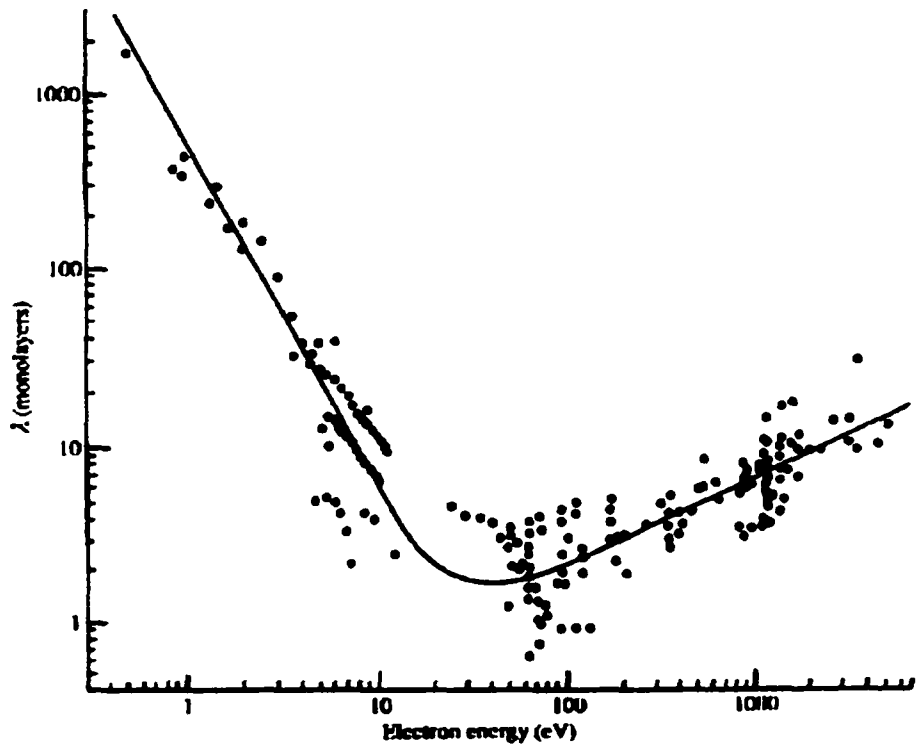

Figure 3.5 This graph shows the mean free path of an electron (in many different materials) versus the kinetic energy. For the energies used for LEED (20eV-500eV) the mean free path is at a minimum (Prutton, 1994).

because low energy electrons have a wavelength that is the same order of magnitude as the lattice spacing. For example, an electron with energy of 54 eV has a wavelength of 1.7 Å (Thornton, 1993). The success of LEED in surface science comes from the surface

sensitivity of low energy electrons. Electrons with energies in the range of 20 eV to 500 eV have a mean free path near 5 Å, therefore those electrons penetrating more than two or three layers have a high probability of being inelastically scattered. Also, the ion-core cross-section for backscattering can be as large as 1 $Å^2$. So that fewer and fewer electrons penetrate the lower layers of atoms. Both of these factors make LEED an ideal technique to probe the structure of surfaces.

Reciprocal Space

The crystal lattice is characterized by the lattice vectors $\mathbf{a}_1$, $\mathbf{a}_2$ and $\mathbf{a}_3$. Any two lattice points are connected by a translation vector

$$\mathbf{T} = \mu_1\mathbf{a}_1 + \mu_2\mathbf{a}_2 + \mu_3\mathbf{a}_3 \tag{3.2}$$

where μ_1,μ_2 and μ_3 are integers. Then any property of the crystal (e.g. electron number density) will be invariant under any translation T, that is

$$n(\mathbf{r} + \mathbf{T}) = n(\mathbf{r}) \tag{3.3}$$

This periodic function can be expressed as a Fourier series. The Fourier expansion in 3D can be written as

$$n(\mathbf{r}) = \sum_{G} n_G \exp(i\mathbf{G}\cdot\mathbf{r}) \tag{3.4}$$

A set of vectors G are defined such that (3.4) is invariant under any translation T. In other words the set of G must satisfy

$$\exp(i\mathbf{G}\cdot\mathbf{T}) = 1 \tag{3.5}$$

The solution to this condition gives a G of the form

$$\mathbf{G} = \eta_1\mathbf{b}_1 + \eta_2\mathbf{b}_2 + \eta_3\mathbf{b}_3 \tag{3.6}$$

where η_1, η_2 and η_3 are integers and the vectors $\mathbf{b}_1$, $\mathbf{b}_2$ and $\mathbf{b}_3$ take the form (Kittel, 1996):

$$\mathbf{b}_1 = \frac{2\pi \mathbf{a}_2 \times \mathbf{a}_3}{V} \tag{3.7a}$$

$$\mathbf{b}_2 = \frac{2\pi \mathbf{a}_3 \times \mathbf{a}_1}{V} \tag{3.7b}$$

$$\mathbf{b}_3 = \frac{2\pi \mathbf{a}_1 \times \mathbf{a}_2}{V} \tag{3.7c}$$

where $V = \mathbf{a}_1 \bullet \mathbf{a}_2 \times \mathbf{a}_3$. Every point on the reciprocal lattice space can then be mapped out by using a reciprocal lattice vector G.

The condition for constructive interference in a one-dimensional array is given by Bragg's law

$$2d \sin\theta = n\lambda \tag{3.8}$$

In 3D this condition can be written as

$$\mathbf{k} + \mathbf{G} = \mathbf{k}' \tag{3.9}$$

The possible diffracted beams in a diffraction experiment can be found by drawing the wave vector **k** of the incident beams which starts at a point called P and terminates at the origin of the reciprocal lattice space. An Ewald sphere is then drawn by drawing a circle around P of radius k (this is shown in Figure 3.6). At any point where the surface of the sphere intersects a lattice point (3.9) is satisfied. This means that the diffraction condition is met. Therefore the incident wave **k** will yield diffracted beams of wave vectors **k'** for every lattice point that intersects the Ewald sphere. Since these diffracted beams are dependent on the reciprocal lattice, any measurement of these beams will provide information on the reciprocal lattice.

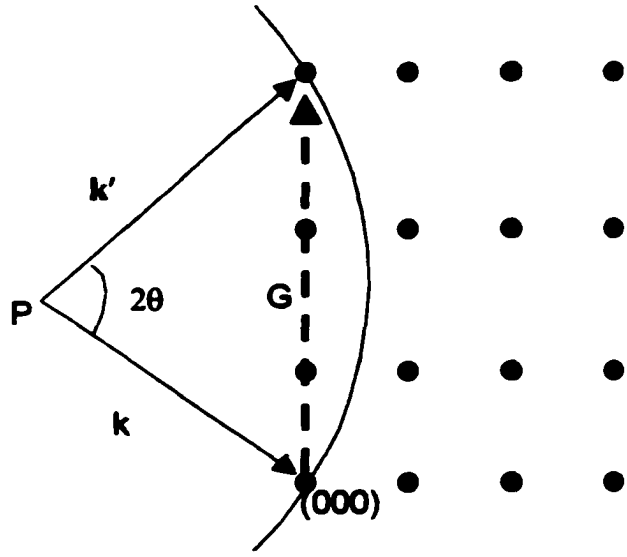

Figure 3.6 The wave vector k of the incident beam is drawn in the reciprocal lattice space. k is drawn so that the vector ends at the origin of reciprocal space. A sphere drawn around P of radius k is the Ewald sphere. From this it is obvious that each diffracted beam is only seen for very specific energies.

The situation is simplified somewhat when using electrons since they essentially only see the first layer. In this case only a 2-D lattice needs to be considered since

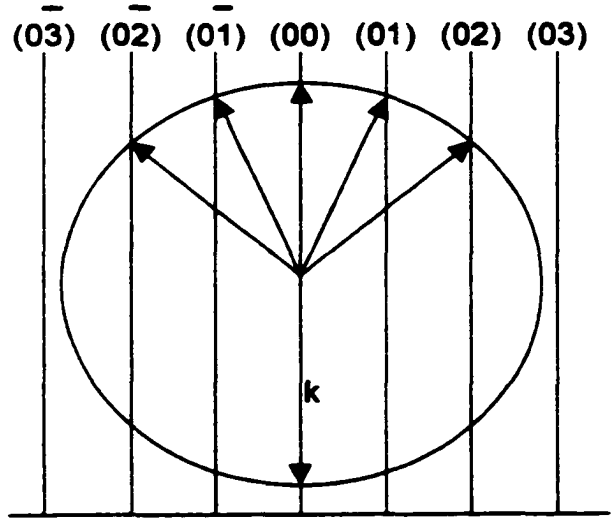

Figure 3.7 The Ewald Sphere shows the 5 backscattered beams from the surface for electrons incident normal to the surface.

scattering from all but the first layer can be neglected. The reciprocal lattice in 2D has reciprocal rods instead of reciprocal points because there is no restriction on the perpendicular component of **k**. Then the condition for diffraction is relaxed to:

$$\mathbf{k}_{//} + \mathbf{G}_{//} = \mathbf{k}'_{//} \tag{3.10}$$

Unlike the 3D case where a certain beam will only occur at certain discrete momentum, in the 2D case a diffraction beam will appear at all momentum provided the corresponding reciprocal rod is in the Ewald sphere.

LEED Set-Up

Figure 3.8 shows the LEED experimental set-up. It consists of an electron gun to

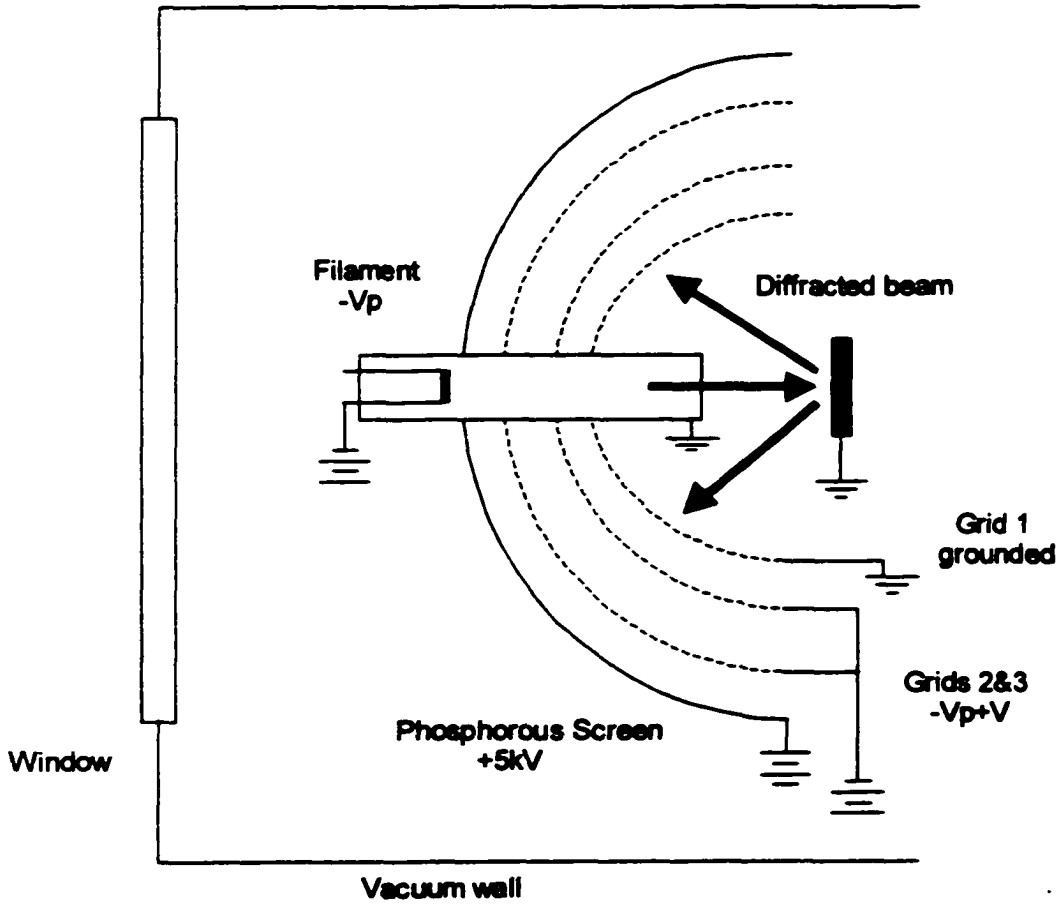

Figure 3.8 This shows how the LEED technique is realized

supply a monochromatic beam of electrons, a series of hemispherical grids and a phosphorous screen to view the diffracted electrons. The filament is biased to $-V_p$ so that the incident electrons have an energy of eV_p. The electrons that are backscattered travel back through grid 1 in a straight line due to the field free region between the grounded sample and the grounded grid 1. Grids 2&3 are biased to a voltage slightly above $-V_p$ to filter out inelastically scattered electrons that have a lower kinetic energy. The screen is biased to a potential of +5 kV to accelerate the electrons and insure that they excite the screen phosphors. A Diffraction pattern appears as bright spots on the phosphorous screen corresponding to the reciprocal lattice of the surface lattice. The diffraction patterns are recorded using a digital camera purchased from Electrim Corporation. The camera stores the digital images directly onto the computer as TIFF files.

Mo(001)

The LEED image of the clean Mo(001) surface yields a 1x1 image. A body-centered cubic crystal and the (001) plane are shown in Figure 3.9.

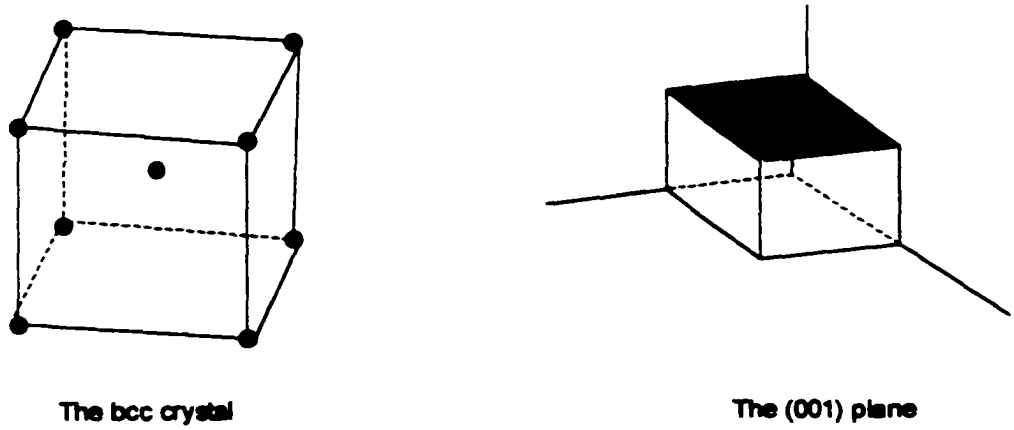

Figure 3.9 The bcc crystal and the (001) plane

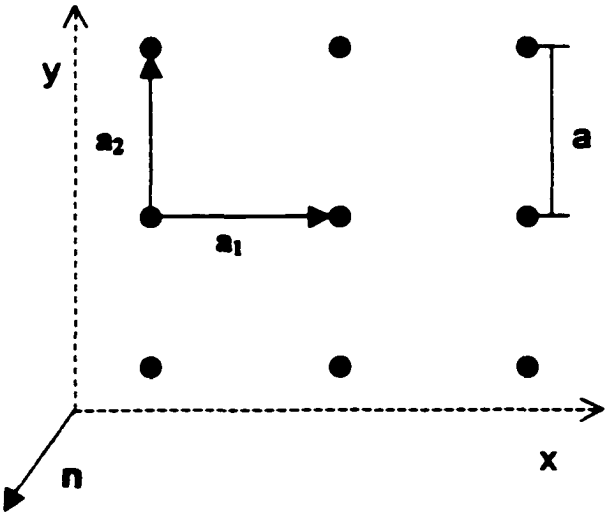

Figure 3.10 The crystal lattice vectors $\mathbf{a}_1$ and $\mathbf{a}_2$

The 2D lattice space of bcc(001) is a square pattern and the lattice vectors can be drawn as shown in Figure 3.10

To transform a 2D real space lattice into the 2D reciprocal space lattice equations (3.7) can be simplified to (Van Hove, 1986):

$$\mathbf{b}_1 = 2\pi\left[\frac{\mathbf{a}_2 \times \mathbf{n}}{\mathbf{a}_1 \bullet (\mathbf{a}_2 \times \mathbf{n})}\right] \qquad (3.11a)$$

$$\mathbf{b}_2 = 2\pi\left[\frac{\mathbf{n} \times \mathbf{a}_1}{\mathbf{a}_2 \bullet (\mathbf{n} \times \mathbf{a}_1)}\right] \qquad (3.11b)$$

where $\mathbf{a}_1$=(a,0,0), $\mathbf{a}_2$=(0,a,0) & $\mathbf{n}$=(0,0,1)

therefore $\mathbf{a}_1 \bullet (\mathbf{a}_2 \times \mathbf{n}) = a^2$

and $\mathbf{a}_2 \times \mathbf{n} = \mathbf{a}_1$

so from (3.11a) $\mathbf{b}_1 = \frac{2\pi}{a}\mathbf{a}_1$

a similar approach using (3.11b) gives $\mathbf{b}_2 = \frac{2\pi}{a}\mathbf{a}_2$

The reciprocal lattice vectors are thus unchanged in direction with magnitude $2\pi/a$. As a result the LEED image of the bcc(001) surface will appear square.

LEED for Quality Check

LEED is a useful tool to determine the periodicity of the crystal but it is not limited to that. Ordered defects such as contaminates will yield superstructures on the LEED image of the substrate. For example if there is oxygen on the surface of the molybdenum sample the LEED image can show an oxygen diffraction pattern superimposed on the substrate's 1x1 pattern. Differing amounts of oxygen on the surface would correspond to different reconstructions (Kan, 1969). Experiments showed that any

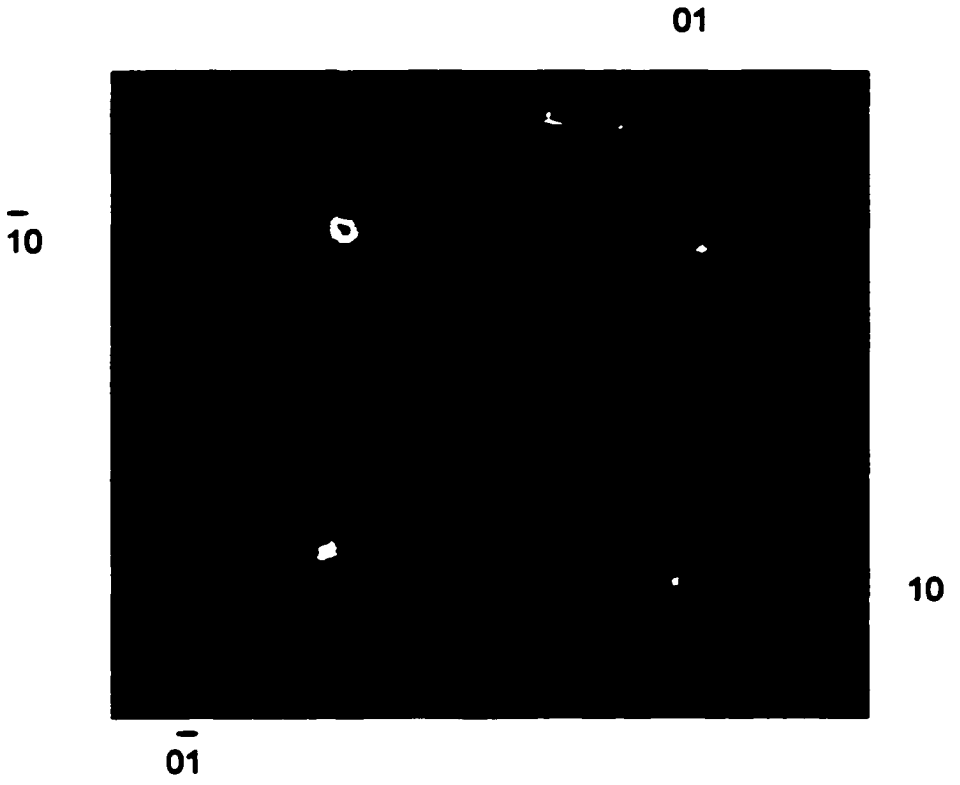

Figure 3.11 A LEED image of the square reciprocal lattice of the clean Mo(001) surface.

amount of oxygen detectable by the LEED was detrimental to the growth of ordered thin films. Any growth on an oxidized Mo surface would only result in diffuse LEED images indicating a disordered film. Any nonperiodic defect or disordered surface will contribute to the diffuse background of the LEED image.

3.3 Auger Electron Spectroscopy

Introduction

Auger Electron Spectroscopy (AES) is a technique that is used to determine the elemental composition of a sample's surface. It can also lead to information about the chemical state of the atoms on the surface. An Auger electron spectrum is a plot of electrons detected as a function of energy. Every element except hydrogen and helium has the ability to emit Auger electrons and can then be identified by the unique position of peaks in the Auger spectra.

The Auger Process

An example of an Auger process is shown in Figure 3.12 and can be explained as follows. An incident electron ionizes an atom by producing a hole in a core level. This deep hole in the core level of the atom is then filled by an electron from a less tightly bound (higher) level and a second electron escapes with the kinetic energy required for energy conservation.

Auger transitions are labeled by the atomic levels of the electrons involved. For example, the Auger process in Figure 3.12 is a KL(II)L(III) or simply a KLL transition. The shells in Auger transition are labelled by x-ray spectroscopy nomenclature where the first three electron shells are labelled K, L and M respectively instead of the optical spectroscopy nomenclature.

The emerging electron will then have a kinetic energy that depends on the energy levels of the atom from which it came. This energy can be roughly approximated by:

$$E \approx E_K - E_{L(II)} - E_{L(III)} \qquad (3.12)$$

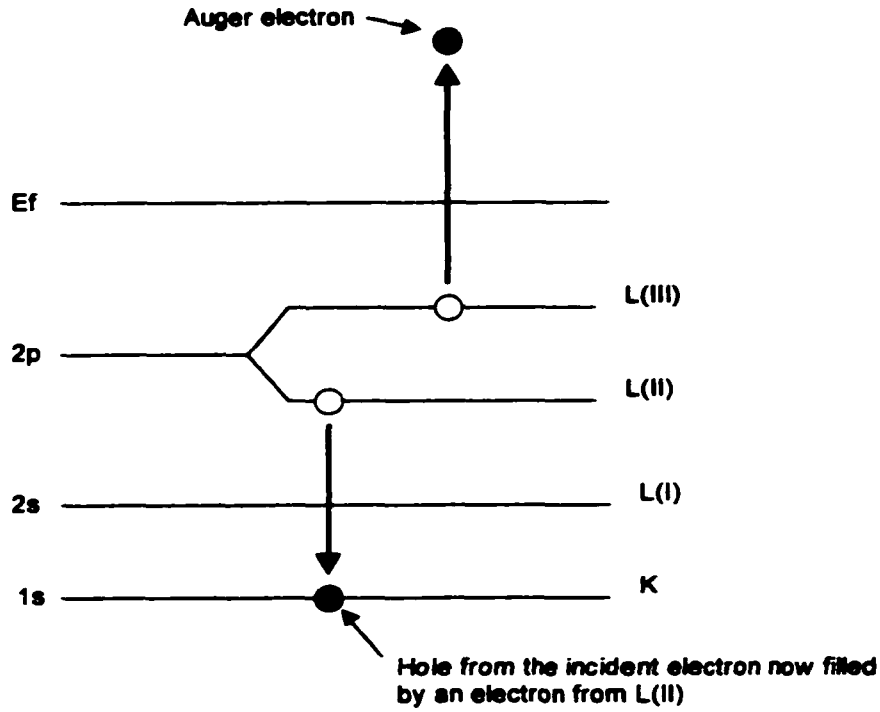

Figure 3.12 An atomic-level diagram of Auger electron emission.

Although more exact calculations may take into account the binding energy in the presence of a core electron hole or the coulomb repulsion energy of the two holes in the final state. Since the Auger electrons are characteristic of the energy levels of the atom that they came from, the kinetic energy of an Auger electron represents a fingerprint of the atom that it originated from. An AES spectra is sensitive to the presence of all elements (except hydrogen and helium) on the surface of a sample. This makes AES very useful in determining the purity or cleanliness of a sample. For example, when looking at the Auger spectra of the clean Mo sample a large peak at 190 eV is expected but a peak of any size at 275 eV or 510 eV indicates that the sample is contaminated with carbon or oxygen respectively. AES can detect as little as 5% of a monolayer of carbon (Prutton, 1994). An Auger spectra is shown in Figure 3.13.

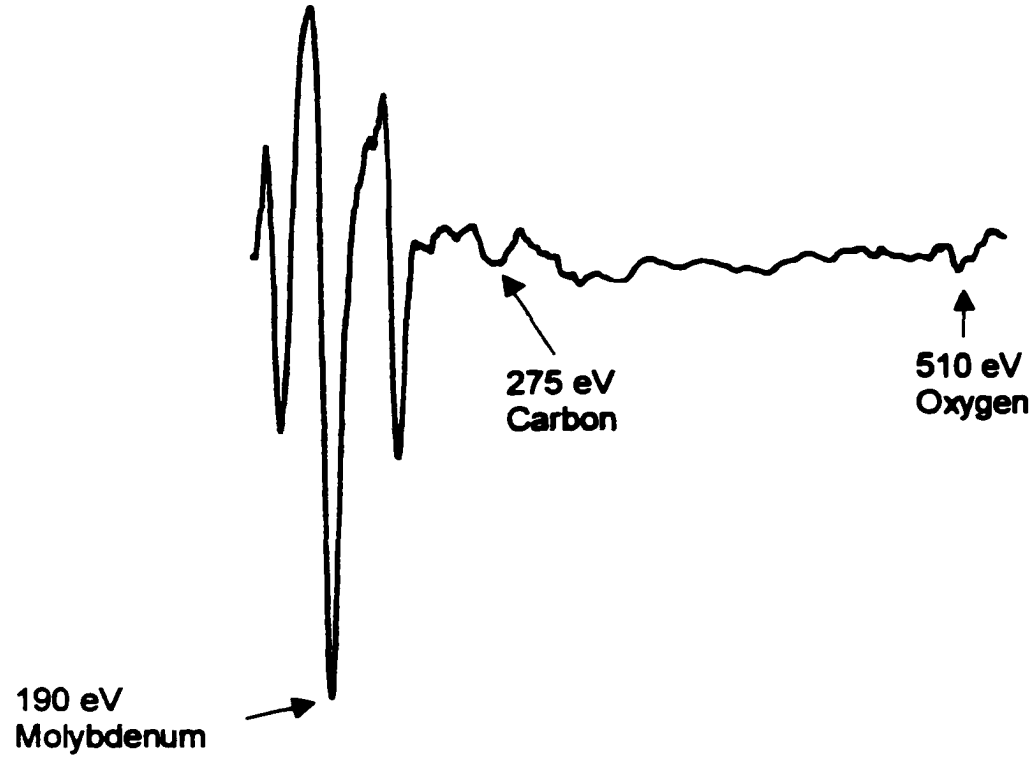

Figure 3.13 An Auger spectra of the Mo sample. The peak at 275 eV and 510 eV shows that there is some carbon and oxygen on the surface

A competing process with Auger electron emission is x-ray fluorescence. In this case when the electron drops down to fill the core vacancy a x-ray photon is emitted with the required energy instead of an electron. However for any element there exists an Auger process such that the excited ions decay predominantly by Auger electron emission instead of x-ray fluorescence. This can be seen in Figure 3.14.

Auger Set-up

There are two commonly used experimental set-ups to perform AES. The Retarding Field Analyzer (RFA) was chosen over the Cylindrical Mirror Analyzer (CMA) since the hardware used for the RFA and that for the LEED are the same.

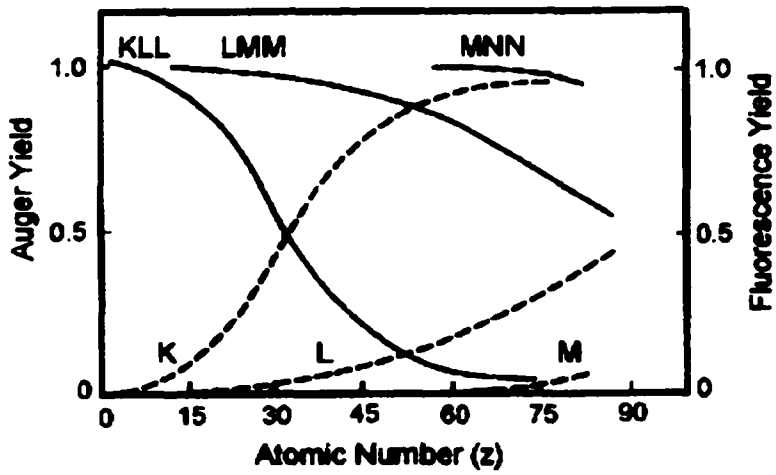

Figure 3.14 A plot of yields versus atomic number. The solid line represent Auger electron emmision while the dashed line represents x-ray fluorescence (Hedberg 1995).

A diagram showing the hardware for AES is shown in figure 3.15. Electrons are emitted from the filament and strike the sample. The Auger electrons that are created and emitted

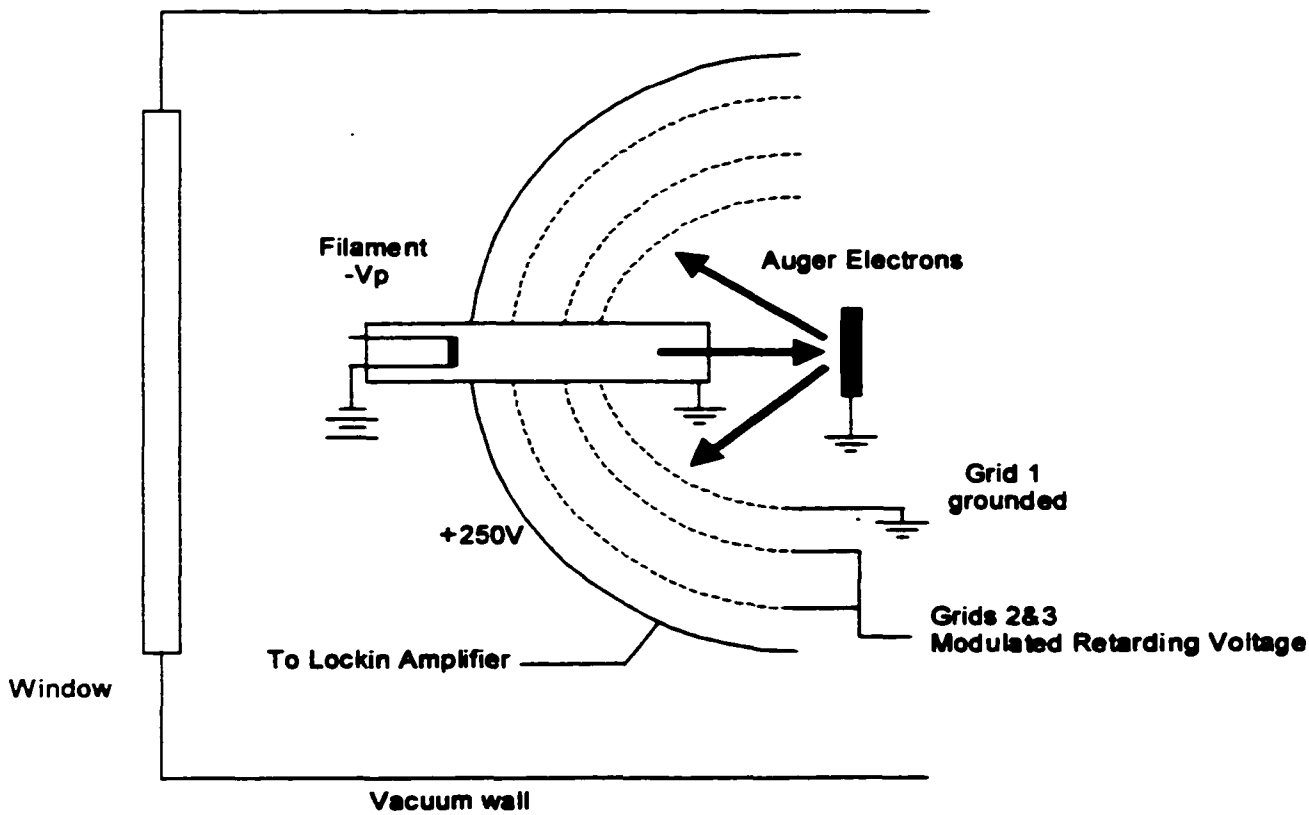

Figure 3.15 This is a schematic of how the RFA optics of a AES are set-up. This is very similar to Figure 3.8 which shows the LEED set-up.

out of the sample will travel through the field free region created by grounding the first grid. The electrons then travel to grids 2 & 3 which are given a modulating voltage around V_0. This is done because all of the electrons with energy greater than eV_0 are detected and the signal measured is:

$$S(E) = \int_{eV_0}^{\infty} N(E)dE \tag{3.13}$$

In order to measure N(E) a modulating voltage $V=V_0+\Delta V\cos\omega t$ is applied and the first derivative of the signal is measured using a lock-in amplifier. The signal current can be expanded as a Taylor series around V_0.

$$S(eV) = S(eV_0) + \left(\frac{dS}{dE}\right)_{eV_0} \Delta(eV)\cos\omega t + \frac{1}{2}\left(\frac{d^2S}{dE^2}\right)_{eV_0} \Delta(eV)^2\cos^2\omega t + \ldots \tag{3.14}$$

using a trigonometric identity to replace $\cos^2\omega t$ the series becomes

$$S(eV) = S(eV_0) + \left(\frac{dS}{dE}\right)_{eV_0} \Delta(eV)\cos\omega t + \frac{1}{4}\left(\frac{d^2S}{dE^2}\right)_{eV_0} \Delta(eV)^2(1+\cos 2\omega t) + \ldots \tag{3.15}$$

Therefore detection of a current at the collector with a frequency of ω (using a phase sensitive detector) gives a current that is proportional to the first derivative of the signal, N(E). Auger transitions show up as small peaks on a N(E) vs. E plot as shown in Figure 3.16. For this reason it is advantageous to plot the dN(E)/dE vs E instead. This is done by detecting current with a frequency of 2ω, which is proportional to the second derivative of the signal. This phase sensitive detection has the additional bonus of measuring signals with small signal to noise ratios. V_0 is ramped through the desired range of energies to give a continuous plot of Auger electron yield versus energy.

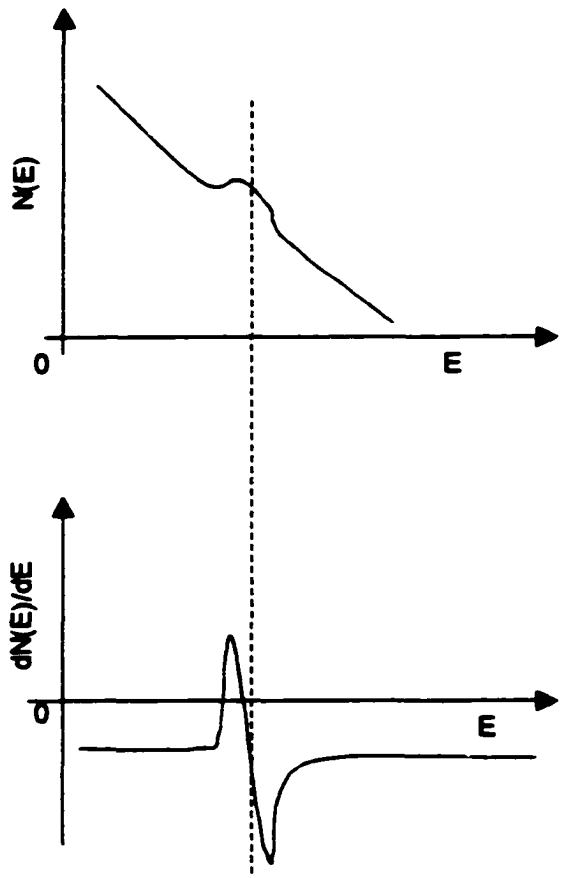

Figure 3.16 The second derivative of the signal, dN(E)/dE, shows more distinct peaks than N(E)

Determining the Growth Mode

AES is often used to study the mode of film growth. Characteristic Auger transitions of the substrate or adsorbate are measured as a function of film coverage. This gives an Auger signal versus time plot called AS-t. Figure 3.17 shows the different AS-t plots for the three distinct growth modes. For FM growth the AS-t plot is a series of straight lines where the breaks occur at the completion of a layer and the beginning of the next (Argile, 1989). The differences in the slopes are due to the attenuation of the signal from an increasing number of absorbate layers and therefore the succeeding layers receive smaller fractions of the original substrate emission. The situation is quite

different for 3D island growth, where during film growth large areas of the substrate can remain deposit free. The substrate signal will then be much less suppressed than the layer by layer case. The AS-t will show a much slower increase in the adsorbate signal and likewise a much slower decrease in the substrate signal. The layer plus island growth mode is the intermediate case where the AS-t will follow a FM curve until there is a distinct break, and the curve will then follow a VW AS-t curve. This break point indicates the transition from layer growth to island growth mode.

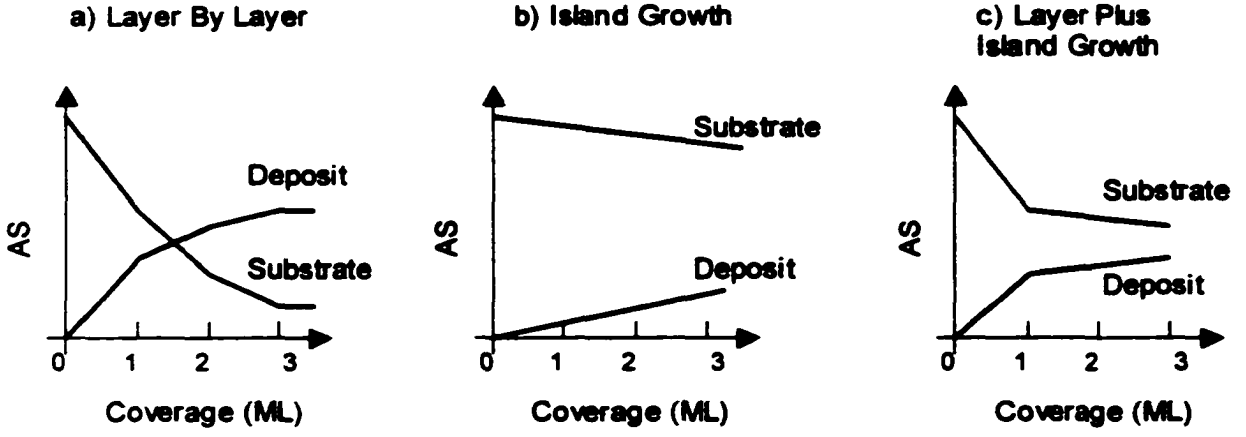

Figure 3.17 The different AS-t plots for the different growth modes.

Thicker films were not grown by evaporating more Mg onto the previous film. Each film was deposited starting from zero coverage. After a film was grown and measured the sample would be flashed to 1100°C to desorb the Mg and MgO from the surface.

CHAPTER 4

Results

Previous Results

Previous results indicate that Mg grows on Mo(001) in a Stranski-Krastanov growth mode at room temperature (Wu, 1992). While in the layer-by-layer mode, Mg grows as pseudomorphic fcc Mg(001). The first two layers grow via island nucleation whereas the next two layers grow by step flow (Gallagher, 1999). After the deposit of 4

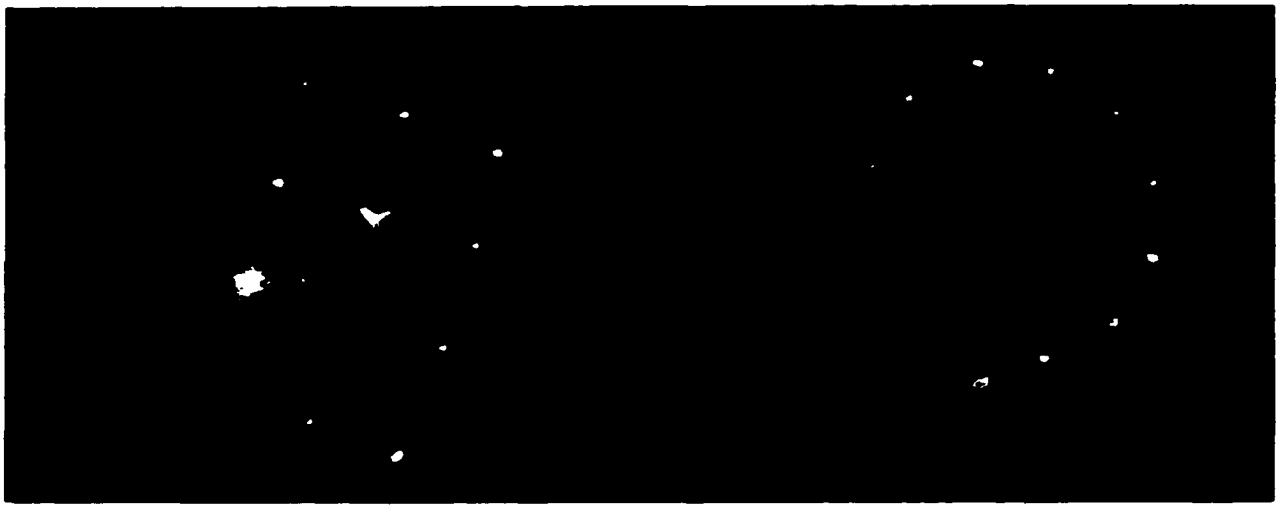

Figure 4.1 The LEED image on the left shows the 1x1 square pattern of a the fcc(001) surface while the image on the right is the hexagonal pattern of the Mg(0001) islands. Figure 4.9 illustrates why this is called a hexagonal pattern.

layers there is a simultaneous transition to 3D island growth and the growth of hcp Mg(0001). Previously, a scanning tunneling microscope was used to find the transition from layer to island growth. Here LEED is used, since the change in growth mode coincides with a change in the structure of the film (Figure 4.1). Fcc Mg(001) shows a 1x1 pattern, while Mg(0001) shows a hexagonal pattern.

Hexagonal Pattern of Mg(0001)

For hexagonal lattices an additional crystallographic axis is defined within the hexagonal basal plane. This additional axis is called i and is denoted by the Miller-Bravais indices (hkil). It follows the simple relationship i = -h-k (Van Hove, 1986). Therefore the (0001) plane could simply be called the (001) plane in the conventional Miller-index notation. The hcp crystal and the (0001) face are shown in Figure 4.2.

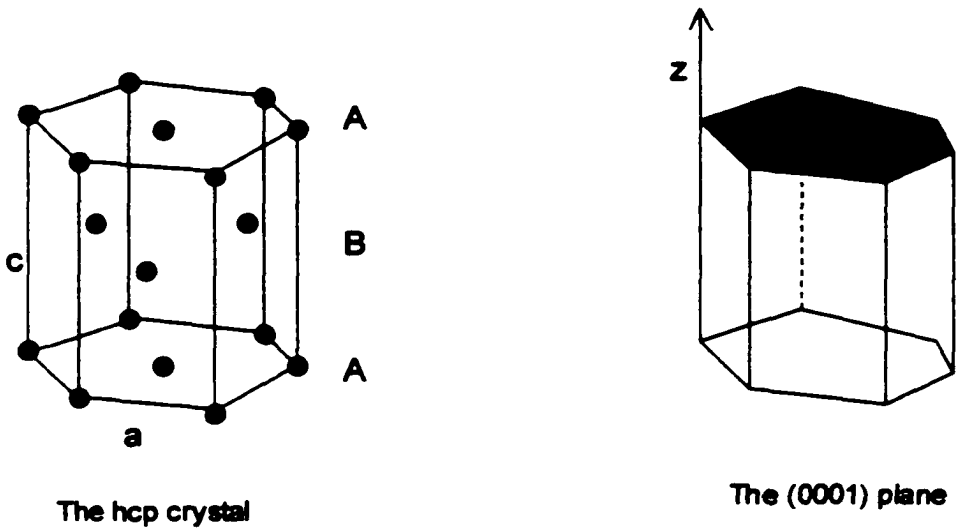

Figure 4.2 The hcp crystal and the (0001) plane

Looking down on the 2D surface of the (0001) plane will give a hexagonal surface. Applying equations (3.11a) and (3.11b) to transform the two real space lattice vectors to reciprocal lattice space yields a hexagonal pattern with a rotation as shown in Figure 4.3.

The LEED image however does not simply show a hexagonal spot pattern, rather it shows the superposition of two hexagonal patterns rotated by 30°. This is because the

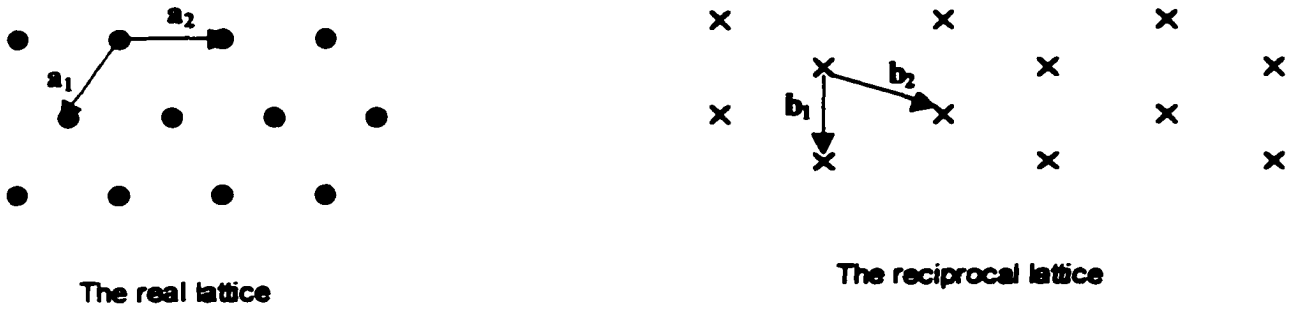

Figure 4.3 Applying the transformation equations to $\mathbf{a}_1$ and $\mathbf{a}_2$ give the new vectors $\mathbf{b}_1$ and $\mathbf{b}_2$

islands grow on the Mo(001) substrate which has fourfold symmetry. This allows for two domains of island growth each rotated by 30° (Figure 4.4).

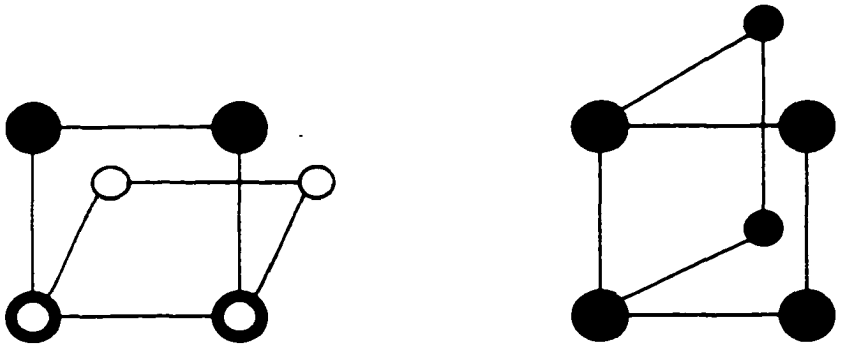

Figure 4.4 The two domains of the film that contribute to the LEED image.

Room Temperature Deposition

An AS-t measuring the Auger intensity of the substrate signal of Mo_{MNN}(190 eV) as well as the deposit signal of Mg_{LMM}(48 eV) is shown in Figure 4.5. The AS-t plot shows a distinct break.

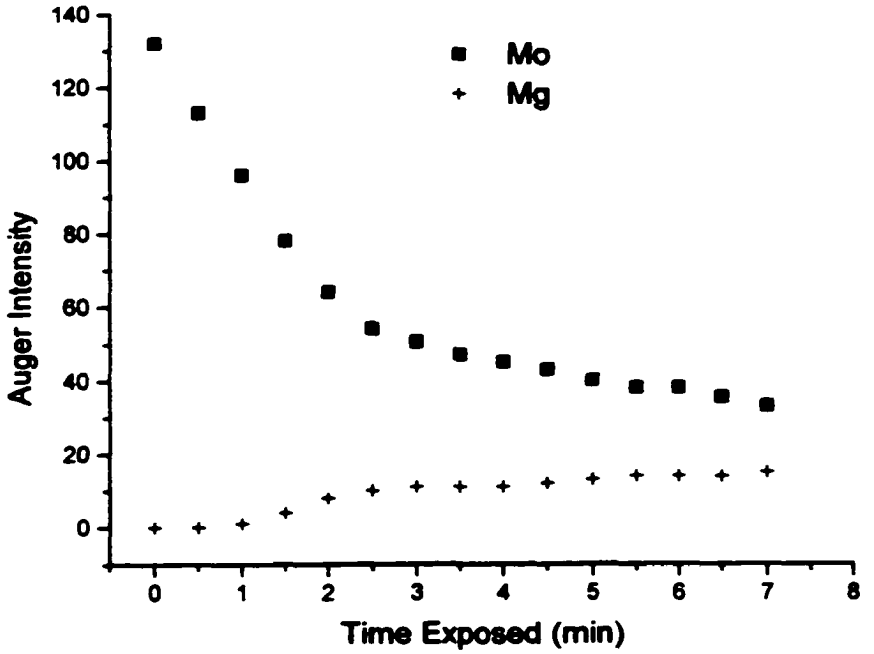

Figure 4.5 AS-t plot showing the distinct break in the decrease of the substrate signal and in the increase of the deposit signal.

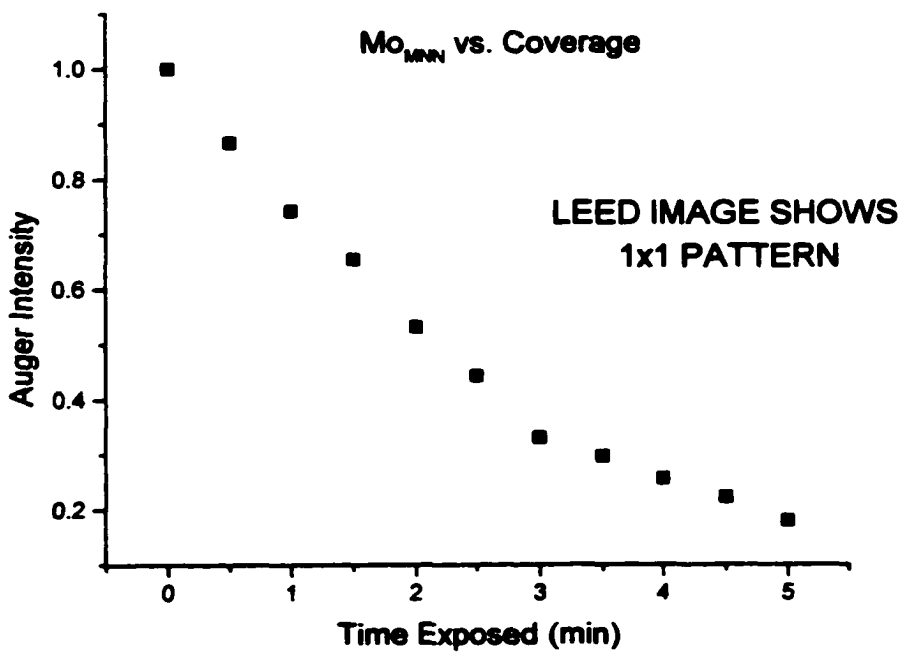

Figure 4.6 AS-t plot with greater resolution showing the break in combination with LEED

A subsequent experiment in which an AS-t plot was taken in combination with LEED images is shown in Figure 4.6. LEED taken after the break still shows a 1x1 pattern, indicating the film is still growing layer-by-layer and that the break is not the transition to island growth. Another AS-t experiment was performed with longer exposure times. The plot is shown in Figure 4.7. The LEED image taken after the second break is shown in Figure 4.8.

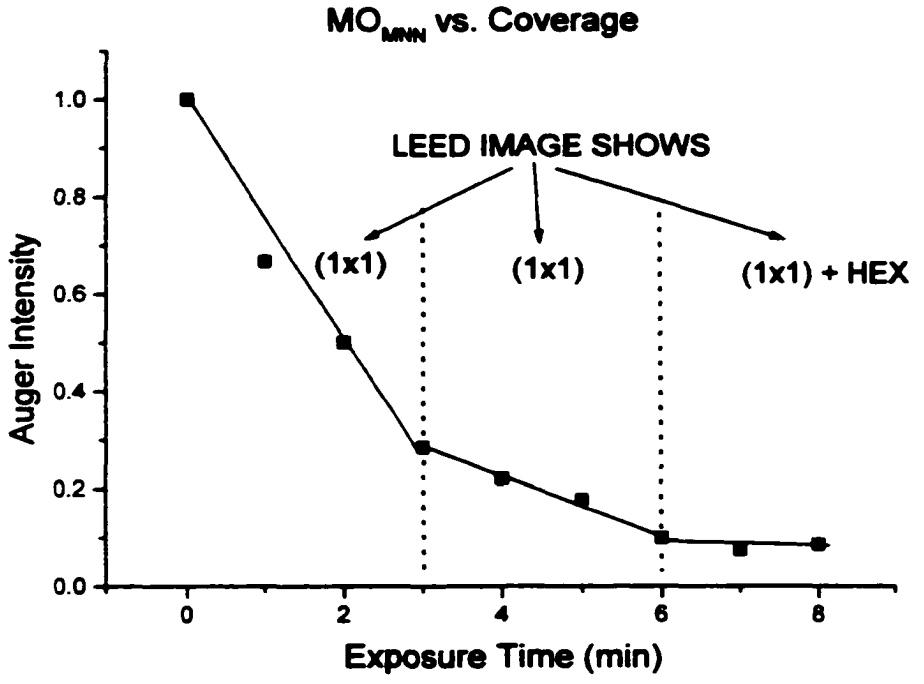

Figure 4.7 AS-t showing two breaks with LEED images taken as shown

This image shows a superposition of the 1x1 pattern of the layer and the hexagonal pattern of the islands as shown in Figure 4.8. The superposition means that the image was taken after the onset of island growth. Since LEED images taken before the second break give only a 1x1 pattern it is concluded that the second break in the AS-t plot of Figure 4.4 is the onset of 3D island growth. Gallagher et al. found the transition to 3D

Figure 4.8 (left) LEED image showing the superposition of a hexagonal pattern on a 1x1 pattern. The negative of the LEED image where the Xs represent spots of the 1x1 pattern and the lines show the two domains of the hexagonal pattern

island growth occurs following the completion of the Mg fourth layer (Gallagher, 1999). The second break in the plot occurs after 6 minutes of exposure and the first break in the plot occurs at half this time. Since the flux was maintained constant, the time exposed to the evaporator is linearly related to coverage. The first break represents the completion of the second layer and the onset of the third. In other words, when the intensity of the Mo Auger peak decreases to 30% of the clean substrate signal there are two monolayers of Mg on the sample.

Throughout the layer growth the 1x1 LEED image did not change. This shows that there is no strain relaxation with increasing thickness of the film.

Different plots were taken at different rates of evaporation (0.5-1ML/min) but the results of the plots are always the same. A distinct break in the curve is always seen when the signal has decayed to 30% of the clean substrate. LEED images taken after this break confirm that this occurs before the transition to 3D growth. If the film is growing layer-by-layer another break at 1.5 min should be seen corresponding to the completion

of the first layer. The AS-t plot for monolayer growth should consist of breaks at the completion of each layer (this is shown in Figure 3.17a). In fact, the break after the completion of the first layer should be more distinct than the break corresponding to the completion of the second layer, however none is seen.

If the initial film growth proceeds by the development of a bilayer then after the equivalent coverage of one monolayer only half of the surface is covered and no break in the AS-t plot would be observed. After an equivalent coverage of two monolayers the first full layer would cover the substrate and subsequent deposition would produce a break in the AS-t plot.

Modeling the Growth

To investigate the possibility of an initial bilayer followed by a monolayer, the growth process was modeled theoretically. The model is also used to show that the first two layers do not grow as a monolayers. The growth of a bilayer followed by another bilayer and the growth of a trilayer followed by a monolayer are not modeled because these are known not to occur. Previous STM studies of the third and fourth layer clearly show that they grow in monolayers (Gallagher, 1999).

Throughout growth of the first layer there are contributions to the Auger signal from the exposed substrate and from the attenuated signal of the covered substrate as shown in Figure 4.9. The overall intensity can be predicted by the exponential attenuation law (Rhead, 1981)

$$I = I_0 \exp(-t/\lambda \cos\theta) \qquad (4.1)$$

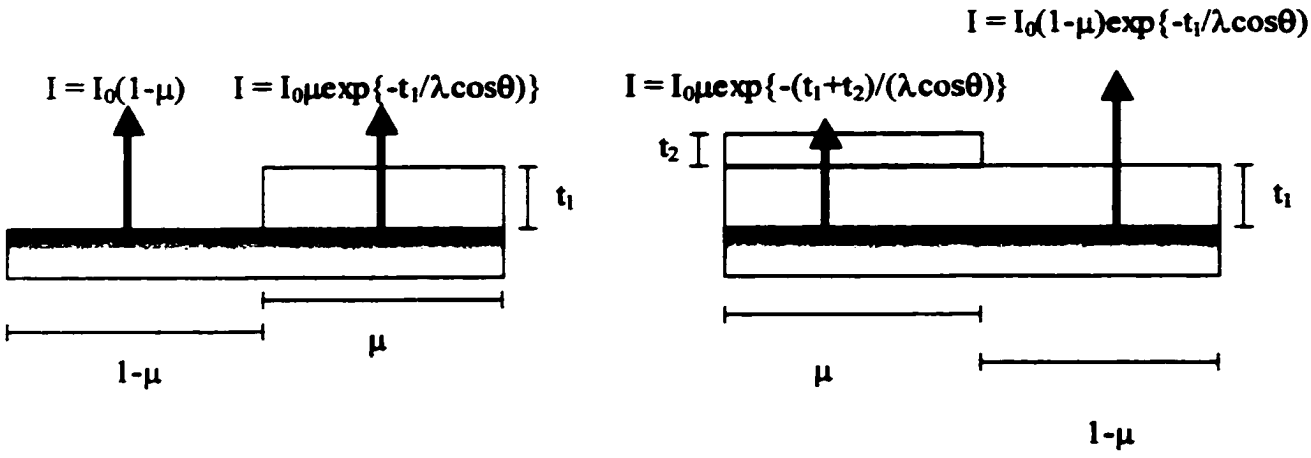

Figure 4.9 Shows the contributions to the Auger signal from the substrate during the growth of the first layer (left) and the growth of the second layer (right).

Where λ is the mean free path of the electron, θ is the mean acceptance angle of the electron detector, t is the thickness of the film and I_0 is the total unimpeded Auger yield. Most of the Auger electrons that are collected are not emitted perpendicular to the surface; as a result most will have had to travel through more of the film. Therefore the effective thickness of the film is $t/\cos\theta$. It was determined that the mean acceptance angle for our LEED instrument was 33°. The decrease in the Auger intensity as a function of coverage μ will be given by

$$I = I_o(1-\mu) + I_0\mu\exp\{-t_1/(\lambda\cos\theta)\} \qquad (4.2)$$

The decay in the Auger intensity for the growth of the second layer can then be calculated in a similar way (shown in Figure 4.9) by the following equation

$$I = I_0(1-\mu)\exp\{-t_1/(\lambda\cos\theta)\} + I_0\mu\exp\{-(t_1+t_2)/(\lambda\cos\theta)\} \qquad (4.3)$$

If the break in the AS-t plot from Figure 4.5 is simply the completion of the first layer then (4.2) and (4.3) can be used to fit the data before and after the break respectively with $I_0=1$ and $t_1=t_2=2.2$ Å. A least squares fit was applied to the data to find

λ. It is determined that, assuming monolayer growth, the mean free path of the electron would have to be 1.9 Å. This is an unphysical result. All previous studies of electrons in various materials give mean free paths between 4 Å and 8 Å at 190 eV. It is concluded that the data does not fit a layer-by-layer growth model.

If the break corresponds to the completion of a bilayer then again (4.2) and (4.3) can be used to fit λ, however now t_1=4.4Å since the first layer is now two monolayers in thickness and t_2 is 2.2 Å. Similar analysis yields an electron mean free path of 4.3Å. This is a reasonable number and suggests that initially Mg grows as a bilayer.

Deposition at Elevated Temperature

AS-t plots were taken throughout the possible temperature range from room

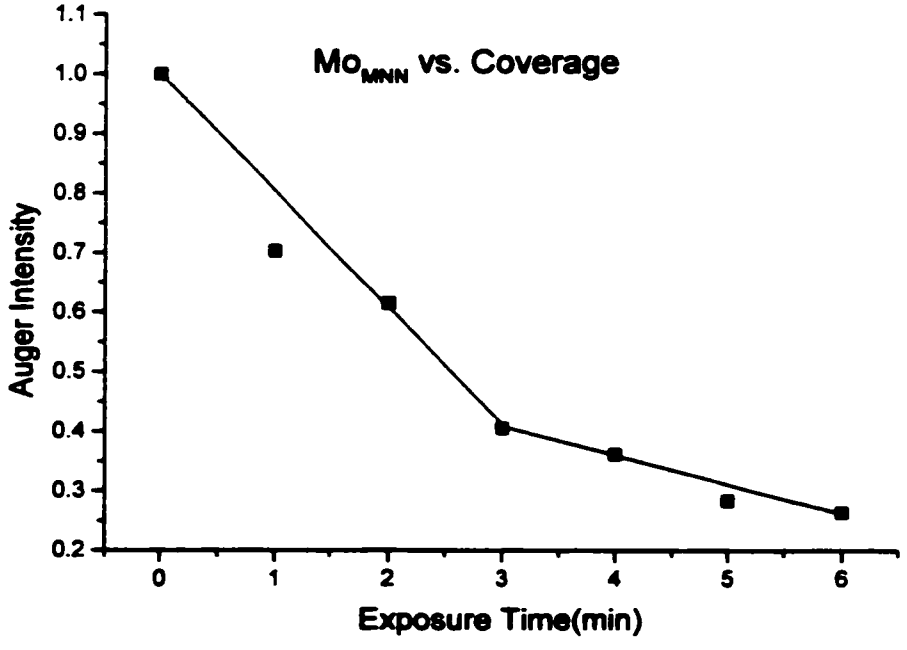

Figure 4.10 AS-t taken at a temperature of 425 K

temperature up to 450 K. No results could be obtained below room temperature because the system did not have cooling capabilities, and results above 450 K could not be obtained since Mg thermally desorbs at 500 K. AS-t plots in this temperature range give similar results to those obtained at room temperature. The AS-t plot shown in Figure 4.10 was measured using a substrate temperature of 425 K.

As well as AS-t plots LEED images were also taken at elevated temperatures to further investigate the transition from layer to island growth. It was found that LEED changes from a 1x1 pattern to a superposition of 1x1 and hexagonal pattern at the same coverage as room temperature. It is concluded that throughout the temperature range investigated the transition from layer to island growth mode always occurs following the completion of the fourth layer.

The initial growth of the bilayer and the transition to island growth after the completion of the fourth layer is unaffected by a change in temperature. This suggests that both of these events are not kinetically limited.

Discussion

Bilayer growth has been observed in other metal on metal systems. Co films grown on Cu(001) grow in bilayer islands (Fassbender, 1997). At thicknesses greater than 2ML the growth proceeds in a layer-by-layer fashion. The explanation for this is that $\gamma_{Co} > \gamma_{Cu}$ and the energy of the system is reduced if more of the substrate surface is left exposed. This creates an energy barrier for interlayer mass transport from the second layer to the first layer. This is not the case for Mg on Mo(001) since $\gamma_{Mg} < \gamma_{Mo}$.

Thermodynamics favours a 2D Mg surface and the difference in surface energies cannot create an energy barrier.

In a study of cobalt films on Au(111) it was found that initially the film forms islands that are two atomic layers high and grow laterally with increasing coverage (Voightländer, 1991). Here bilayer growth is attributed to the large lattice mismatch between Co and Au (14%). The large lattice mismatch leads to substantial lattice strain. The film is more relaxed in the second layer, thus growing in a bilayer reduces the total strain energy of the film. For the growth of Mg on Mo(001) the lattice mismatch is only 2%. The strain energy of the film would therefore not be significantly reduced by growing in a bilayer.

Low temperature growth of Pb on a strained Pb monolayer results in the growth of a complete bilayer followed by a layer-by-layer regime (Bocquet, 1997). In this study LEED observations suggest that the strain is fully relaxed by the bilayer. This is quite different from our system where LEED images show that there is no relaxation of strain after the completion of the bilayer.

Different adatom mobilities and therefore different nucleation densities on successive layers due to strain can considerably affect the growth morphology. This is seen in the transition from island nucleation to step flow in the growth of Mg on Mo(001) (Gallagher, 1999). Mg atoms adsorbed onto the Mo surface have a small diffusion constant due to the highly corrugated surface potential of the bcc surface. The low rate of diffusion means that atoms that condense on the Mo surface will nucleate many small islands. With many small islands a significant number of atoms will arrive on top of the islands prior to coalesence. Atoms that adsorb on top of the islands are hindered from

descending onto the Mo surface by a Mg step-edge barrier (Hwang, 1997). The additional barrier leads to the build up of adatoms in the second layer prior to the completion of the first layer. The presence of these atoms in the second layer would

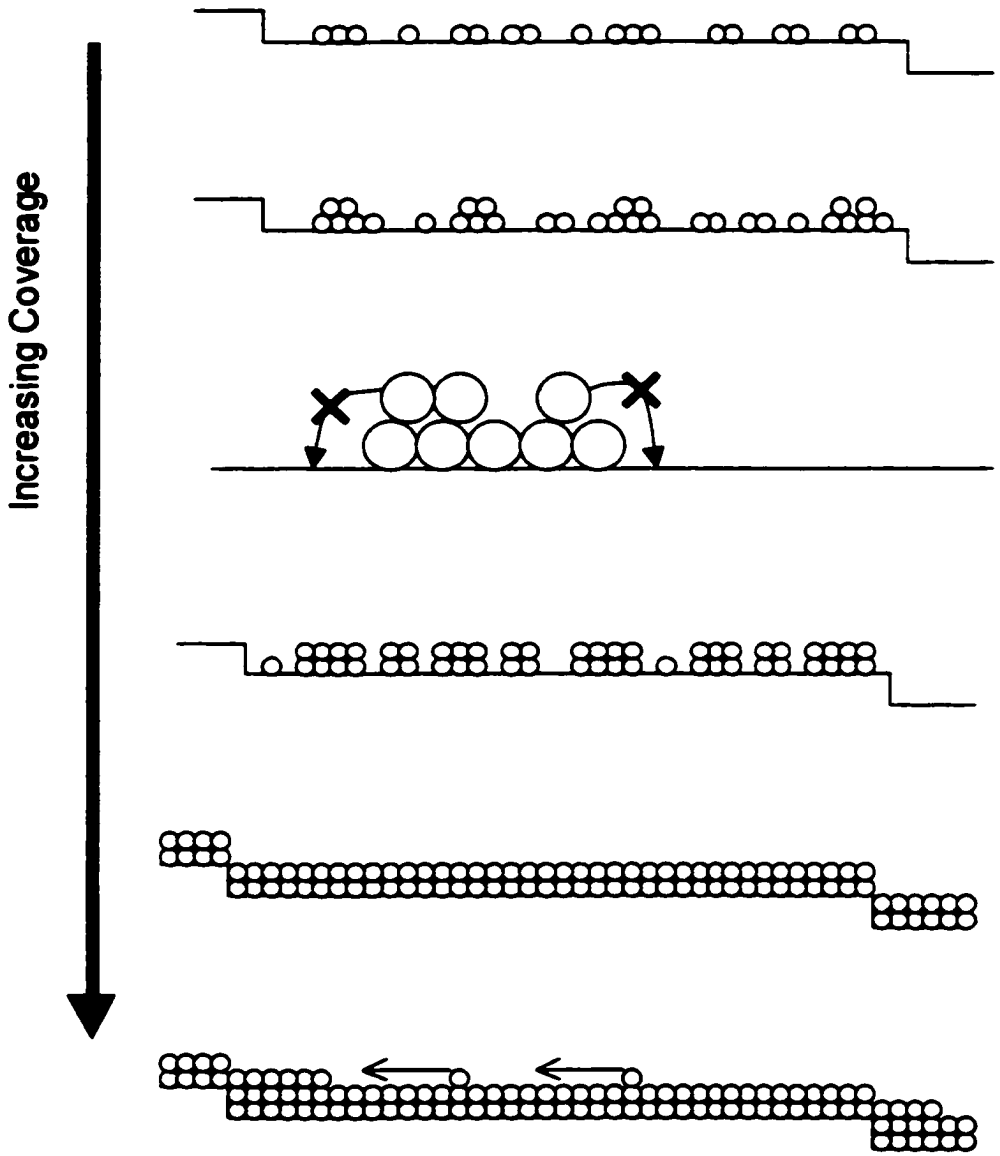

Figure 4.11 The growth of the first few layers of Mg on Mo(001)

eliminate the observation of a break in the AS-t plot following one monolayer equivalent coverage. Once the bilayer is complete lattice compression reduces the corrugation of the surface potential and adatoms on the second layer will have a larger diffusion constant (Brune, 1995). This allows the third and fourth layers to grow by step flow, despite the step edge barrier. This increased diffusion constant results in the step flow growth of the third and fourth layer of the film. The evolution of the Mg film on the Mo substrate for the first few layers of coverage is shown in Figure 4.11.

CHAPTER 5

Conclusion

The decrease in the AS-t plot of the Mo signal as Mg is deposited shows two distinct breaks. Using LEED images it was found that this first break is not the transition from 2D layer growth to 3D island growth. In fact this break occurs after the completion of the second layer while the film is still in the 2D layer growth regime. It is argued that this break corresponds to the completion of an initial bilayer and the onset of the third monolayer. A second break is seen in the AS-t plot after the completion of the fourth layer and LEED shows that this corresponds to the transition from layer growth to island growth. The growth is also modeled for single layer growth and the data is fit to the model. If the first break in the AS-t plot were simply the completion of the first monolayer than the mean free path of the electron would be an unphysical 1.9 Å. A similar curve fit shows that if the first break corresponds to the completion of the bilayer then λ=4.4 Å which is reasonable.

The growth of the bilayer followed by layer growth is attributed to a combination of low Mg diffusion constant on the Mo(001) surface and the presence of a energy barrier that hinders the transfer of atoms between Mg layers. This results in a significant fraction of the islands being two layers high prior to coalesence.

The change in the growth process between the bilayer growing via island nucleation and the third and fourth layer growing via step flow is attributed to a change in mobilities due to the strained film. The strain is a result of the 2% lattice mismatch between the Mg and Mo. Previous computations show that a mismatch of only 2% is sufficient to cause this effect (Brune, 1995).

References

Argile, C. & Rhead, G.E. (1989). *Surf. Sci. Rep.* **10**, 277.

Bauer, E. (1982). *Appl. Of Sur. Sci.* **11/12**, 479.

Bauer, E. (1958). *Z. Kristallogr.* **110**, 423.

Bocquet, F., Robert, S., Gauthier, S., Duvault, J. L. & Klein, J. (1997). *Surf. Sci.* **392**, 86.

Brune, H., Bronmann, K., Röder, H. & Kern, K. (1995). *Phys. Rev. B.* **52**, R14380.

de la Figuera, J., Prieto, J. E., Ocal, J. & Miranda, R. (1993). *Phys. Rev. B.* **47**, 13043.

Esch, S., Hohage, M., Michely T. & Comsa, G. (1994). *Phys. Rev. Lett.* **72**, 518.

Fassbender, F., Allenspach, R. & Dürig, U. (1997). *Surf. Sci Lett.* **383**, L742.

Hedberg, C., A. (1995). *Handbook of Auger Electron Spectroscopy*, 3 edn. Physical Electronics: Eden Prairie Mn.

Gallagher, M. C., Fyfield, M. S. & Joyce, S. A. (1999). *Phys. Rev. B.* **59**, 2346.

Henzler, M. (1996). *Surf. Sci.* **357-358**, 809.

Hwang, R.Q. & Bartelt, M.C. (1997). *Chem. Rev.* **97**, 1063

Kan, H. K. A. & Feuerstein, S. (1969). *J. of Chem. Phys.* **50**, 3618.

Kittel, C., (1996). *Introduction to Solid State Physics*, 7 edn. John Wiley & Sons: Toronto.

Kunkel, R., Poelsema, B., Verheij, L.K. & Comsa, G. (1990). *Phys. Rev. Lett.* **65**, 733.

Lagally, M.G., (1990). *Kinetics of Ordering and Growth at Surfaces*. Plenum Press: New York.

Luth, H., (1993). *Surfaces and Interfaces of Solids*, 2 edn. Springer-Verlag: New York.

Merwe, J. H., Tonsing, D.L. & Stoop, P.M. (1994). *Surf. Sci.* **312**, 387.

Meyer, J. A., Schmid, P. & Behn, R. J. (1995). *Phys. Rev. Lett.* **74**, 3864.

O'Hanlon, J., (1989). *A User's Guide to Vacuun Technology*, 2 edn. John Wiley & Sons: Toronto.

Omega Engineering, (1995). *The Temperature Handbook* Vol. 29. Omega Engineering: Stamford CT.

Prutton, M., (1994). *Introduction to Surface Physics*. Clarendon Press: Oxford.

Schroder, J., Gunther, C., Hwang, R.Q. & Behn,R.J. (1992). *Ultramicroscopy*. **42-44**, 475.

Stanford Research Systems, (1996). *1996-1997 Scientific and Engineering Instruments*. Stanford Research Systems: Sunnyvale, CA

Thornton, S.T. & Rex, A. (1993). Modern Physics for Scinetists and Engineers. Saunders College Publishing: Toronto.

Varian Vacuum Products, (1997). *1997-1998 Catalog*. Varian Associates: Lexington, MA

Van Hove, M.A., Weinberg, W., H. & Chan, C.-M. (1986). *Low-Energy Electron Diffraction*. Springer-Verlag: New York.

Venables, J.A., Spiller, G.D.T. & Hanbucken, M. (1984). *Rep. Prog. Phys.* **47**, 399.

Vitos, L., Ruban, A.V., Skriver, H.L. & Kollár, J. (1998). *Surf. Sci.* **411**, 186.

Voigländer, B., Meyer, G. & Amer, N. M. (1991). *Phys Rev B*. **44**, 10354.

Wu, M.-C., Corneille, J. S., Estrada, C. A., He J.-W. & Goodman, D. W. (1991). *Chem. Phys. Lett.* **182**, 472

Wu, M.-C., Corneille, J. S., He, J.-W., Estrada, C. A. & Goodman, D. W. (1992). *J. Vac. Sci. Technol.* **A10**, 1467.

Yagi, K., Takayanagi, K., Kobayashi, K., Osakabe, N., Tanishiro, Y. & Honjo, G. (1979). *Surf. Sci.* **86**, 174.

Zangwill, A. (1988). *Physics At Surfaces*. Cambrige University Press: Cambridge.